Monthly Notices
of the
ROYAL ASTRONOMICAL SOCIETY

MNRAS **460,** 1059–1076 (2016)
Advance Access publication 2016 May 1

doi:10.1093/mnras/stw1030

The spatially resolved dynamics of dusty starburst galaxies in a $z \sim 0.4$ cluster: beginning the transition from spirals to S0s

H. L. Johnson,[1⋆] C. M. Harrison,[1] A. M. Swinbank,[1,2] R. G. Bower,[1,2] Ian Smail,[1,2] Y. Koyama[3] and J. E. Geach[4]

[1]*Centre for Extragalactic Astronomy, Department of Physics, Durham University, South Road, Durham DH1 3LE, UK*
[2]*Institute for Computational Cosmology, Department of Physics, Durham University, South Road, Durham DH1 3LE, UK*
[3]*Subaru Telescope, National Astronomical Observatory of Japan, 650 A'ohoku Place, Hilo, HI 96720, USA*
[4]*Centre for Astrophysics Research, Science and Technology Research Institute, University of Hertfordshire, Hatfield, Hertfordshire AL10 9AB, UK*

Accepted 2016 April 28. Received 2016 April 9; in original form 2016 February 18

ABSTRACT

To investigate what drives the reversal of the morphology–density relation at intermediate/high redshift, we present a multiwavelength analysis of 27 dusty starburst galaxies in the massive cluster Cl 0024+17 at $z = 0.4$. We combine Hα dynamical maps from the VLT/FLAMES multi-IFU system with far-infrared imaging using *Herschel*/SPIRE and millimetre spectroscopy from IRAM/NOEMA, in order to measure the dynamics, star formation rates and gas masses of this sample. Most galaxies appear to be rotationally supported, with a median ratio of rotational-support to line-of-sight velocity dispersion $v/\sigma \sim 5 \pm 2$, and specific angular momentum $\lambda_R = 0.83 \pm 0.06$ – comparable to field spirals of a similar mass at this redshift. The star formation rates of 3–26 $M_\odot$ yr^{-1} and average ^{12}CO-derived gas mass of $\sim 1 \times 10^{10}$ $M_\odot$ suggest gas depletion time-scales of ∼1 Gyr (∼0.25 of the cluster crossing time). We derive characteristic dust temperatures (mean $T_d = 26 \pm 1$ K) consistent with local galaxies of similar far-infrared luminosity, suggesting that the low-density gas is yet to be stripped. Taken together, these results suggest that these starbursts have only recently accreted from the field, with star formation rates likely enhanced due to the effects of ram pressure. In order to make the transition to cluster S0s these galaxies must lose ∼40 per cent of their specific angular momentum. We suggest this must occur ≥1 Gyr later, after the molecular gas has been depleted and/or stripped, via multiple tidal interactions with other cluster members.

Key words: galaxies: evolution – galaxies: starburst.

1 INTRODUCTION

Rich clusters present a unique laboratory for studying the interaction between galaxies and their local environment. It has long been established that strong trends exist between the morphology, gas content and star formation of cluster galaxies, and the density of the neighbourhood in which they reside. The populations of rich clusters at $z = 0$ are dominated by passive, gas-poor ellipticals and S0s, with star formation all but extinguished in central regions (the morphology–density relation e.g. Dressler 1980; Bower, Lucey & Ellis 1992; Lewis et al. 2002; Kodama et al. 2004; Bamford et al. 2009). However, observations of clusters at intermediate redshift show a striking increase in the fraction of blue star-forming galaxies in cluster cores, from almost zero in the present day to ∼20 per cent by $z \sim 0.4$ (e.g. Butcher & Oemler 1978). This evolution is accompanied by another key evolutionary change: a sharp decline in the proportion of S0 galaxies (Dressler et al. 1997; Poggianti et al. 2009). Studies of emission line and luminous infrared-selected galaxies out to $z \sim 1.5$ have confirmed that star-forming galaxies in fact make up the majority of the population in high-redshift clusters (Tran et al. 2010; Smail et al. 2014). This increase in the number of star-forming galaxies and decrease of cluster S0s with increasing redshift strongly implies that the two populations are linked in an evolutionary scenario.

An important realization was that a large fraction of quiescent cluster members have suffered starburst activity in the recent past. Spectroscopic surveys have identified a significant population of k+a or 'post-starburst' galaxies which appear to be more prevalent with increasing redshift (e.g. Couch & Sharples 1987; Poggianti et al. 1999; Pracy et al. 2005; Swinbank et al. 2007; Tran et al. 2007; De Lucia et al. 2009; Rodríguez Del Pino et al. 2014). Their spectra show strong Balmer absorption lines associated with the recent formation of massive A stars (≤1 Gyr ago), but a lack

⋆ E-mail: h.l.johnson@dunelm.org.uk

of emission lines suggesting the burst was rapidly quenched (e.g. Poggianti et al. 1999; Poggianti & Wu 2000). However, difficulties arise when attempting to link these galaxies to the formation of S0s. Insufficient numbers of strong starbursts are detected in the optical to explain the post-starburst phase, and the luminosities of S0s are in fact substantially brighter than the proposed progenitor spirals (Poggianti et al. 1999; Kodama et al. 2004; Burstein et al. 2005; Sandage 2005). These problems could both be solved if a considerable fraction of starburst activity is heavily obscured. Indeed, deep mid-infrared observations of intermediate redshift clusters with *Spitzer* and *Herschel* have revealed an abundance of such dusty star-forming galaxies which are missing from optical studies (e.g. Coia et al. 2005; Geach et al. 2006, 2009; Elbaz et al. 2007; Marcillac et al. 2007; Koyama et al. 2008; Oemler et al. 2009; Kocevski et al. 2011; Alberts et al. 2014). In an era in which clusters were still accreting much of their mass, there not only appears to be a significant population of star-forming galaxies, but also many with their star formation temporarily enhanced in this dense environment.

In a model where spirals transition to S0s, the star formation of infalling galaxies must be rapidly quenched, their gas discs stripped, and the dynamics transform from rotationally supported discs (high angular momentum) to dispersion dominated spheroids (low angular momentum). Several authors also suggest that the bulge luminosity and bulge to disc ratio of S0s is too large for them to have evolved from spirals by disc fading alone (Dressler 1980; Simien & de Vaucouleurs 1986; Kodama & Smail 2001; Christlein & Zabludoff 2004; Cortesi et al. 2013), and spectral decomposition of local lenticulars has revealed that bulges have younger and more metal-rich stellar populations than their adjacent disc (Johnston, Aragón-Salamanca & Merrifield 2014). It may be that a final, circumnuclear starburst is a critical stage in the transition between infalling spirals and passive S0s. The observational challenge is to identify the processes which may drive this transformation.

Several potential mechanisms are usually invoked to explain galaxy transformations in local clusters: interactions with the intracluster medium (ICM) such as ram pressure stripping, strangulation and thermal evaporation (Kenney, van Gorkom & Vollmer 2004; McCarthy et al. 2008; Merluzzi et al. 2013; Fumagalli et al. 2014; Peng, Maiolino & Cochrane 2015), and tidal interactions, harassment, minor mergers or halo stripping (Mastropietro et al. 2005; Bekki 2009; Smith, Davies & Nelson 2010; Eliche-Moral et al. 2012; Bialas et al. 2015). What remains elusive is the relative contribution of each process, and an understanding of how the time-scales they operate on vary with cluster mass and size (hence redshift), as well as the stellar, halo and gas mass of the infalling galaxy (e.g. Boselli & Gavazzi 2006, 2014).

It is important to study cluster galaxies over a range in redshift to thoroughly explore the mechanisms described above, and to understand what drives the reversal of the morphology–density relation. For example, due to the increased gas fractions of galaxies at high redshift (e.g. Tacconi et al. 2010; Geach et al. 2011), the initial compression of the interstellar medium (ISM) may be more likely to enhance the star formation (Quilis, Moore & Bower 2000; Hopkins et al. 2006; Bekki 2014; Sales et al. 2015). Due to the lower mass of typical clusters (compared to those at $z \sim 0$), the lower ram pressure from the ICM may also result in the starbursts being both more intense, and long lived. Tidal forces from increased galaxy–galaxy interaction rates in rapidly assembling clusters may also destabilize the gas discs, causing a burst of star formation, and a morphological and dynamical transformation.

Identifying cluster starbursts and measuring their dynamics, star formation rates (SFR) and molecular gas properties appears to be key to unravelling the complexities of galaxy evolution in clusters. The short lifetime of the starburst activity provides a snapshot of galaxies which may be undergoing a transition, allowing us to search for potential triggers. For example, asymmetric gas discs may provide evidence for ram pressure stripping (Bekki 2014), high dust temperatures (compared to galaxies in the field) may imply that the cold gas/dust has been stripped (e.g. Rawle et al. 2012), whilst galaxy–galaxy interactions (mergers) may result in complex kinematic signatures (Mihos & Bothun 1998; Colina, Arribas & Monreal-Ibero 2005) depending on the interaction stage and nature of the system (Bellocchi et al. 2013; Hung et al. 2016). Complementing the dynamics with observations of molecular gas also allows us to infer the likely time-scales for the starbursts and measure how long the starburst can be maintained.

In this paper we present a multiwavelength study of 28 spectroscopically confirmed, 24 μm-bright galaxies within Cl 0024+17. This pilot study forms part of a wider investigation into the properties of cluster starburst galaxies. Analysis of our full sample of ~ 150 galaxies observed with FLAMES/KMOS, from 10 massive clusters between $0.2 < z < 1.5$, will be presented in paper II. We measure the morphologies and dynamics of the galaxies using *HST* and VLT/FLAMES multi-IFU observations, respectively, infer SFR from far-infrared observations with *Herschel*/SPIRE and measure molecular gas masses using ^{12}CO(1−0) emission from NOEMA. As an original 'Butcher & Oemler' cluster, Cl 0024+17 has a significant population of blue, star-forming galaxies, and is one of the best-studied clusters at intermediate redshift ($z = 0.395$), with a virial mass $M_{\rm vir} = (1.2 \pm 0.2) \times 10^{15}\ {\rm M}_{\odot} h^{-1}$ (Umetsu et al. 2010), and X-ray luminosity of $L_{\rm X} \sim 2.9 \times 10^{44}$ erg s^{-1} (Zhang et al. 2005). With a rich variety of star-forming galaxies in the cluster, and multiwavelength ancillary data, Cl 0024 provides a useful pilot study for investigating the properties of dusty starbursts in galaxy clusters.

The structure of this paper is as follows. In Section 2, we describe the target selection, observations and data reduction. In Section 3, we describe the galaxy integrated properties, such as SFR, stellar and gas masses, and dust temperatures. In Section 4, we describe the internal properties of the galaxies from the IFU observations: Hα dynamics, two-dimensional maps of star formation, rotation velocity and line-of-sight velocity dispersion. We then explore the properties of these dusty starbursts in the context of their environment, comparing to field spirals and local lenticulars and searching for trends as a function of cluster radius. We consider which mechanisms may have already acted upon these galaxies, and discuss what remains to be achieved to complete the transition to S0s, in Section 5. Finally, Section 6 summarizes our main results. Throughout this paper we assume a ΛCDM cosmology with parameters $\Omega_{\rm m} = 0.27$, $\Omega_{\Lambda} = 0.73$ and $H_0 = 72$ km s^{-1} Mpc^{-1}. The average seeing for our IFU observations, 0.5 arcsec, corresponds to a physical scale of 2.6 kpc at $z \sim 0.4$. Unless otherwise stated, all magnitudes are quoted on the AB system.

2 TARGET SELECTION, OBSERVATIONS AND DATA REDUCTION

2.1 Cl 0024+17

Cl 0024+17 is a well-studied cluster with extensive archival multiwavelength imaging and spectroscopy, and its large population of blue star-forming galaxies makes it an ideal environment for

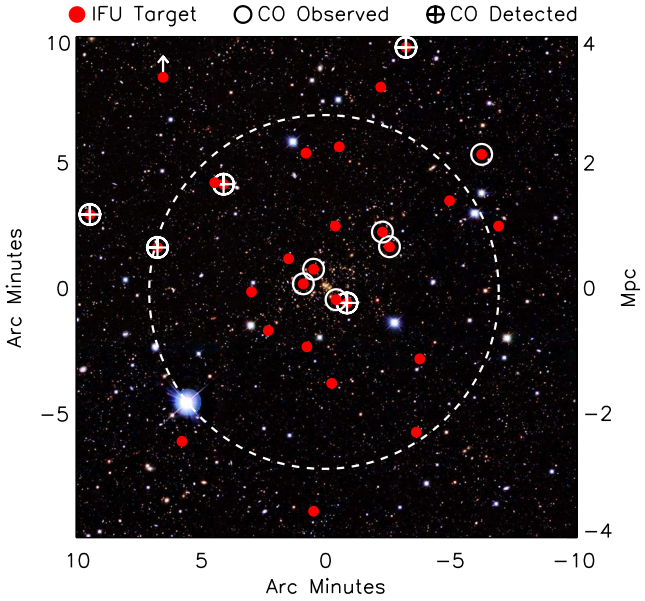

Figure 1. Subaru SuprimeCam *BVI*-colour image of Cl 0024+17, centred on α: 00:26:36.0 δ: +17:08:36 (J2000). The dashed line represents the virial radius of the cluster, $R_{\rm vir} = 1.7$ Mpc. We highlight the 28 spectroscopically confirmed dusty starbursts which were observed using the FLAMES multi-object IFU. Our targets have projected cluster-centric radii of 0.2–3.9 Mpc. We circle galaxies also observed using IRAM PdBI, with crosses to indicate $>5\,\sigma$ ^{12}CO(1−0) detections. It appears that galaxies further from the cluster centre are perhaps more likely to be detected in CO (also see Fig. 2).

exploring the properties of cluster starbursts. In optical wavelengths Cl 0024 appears fairly unremarkable, with a well-concentrated mass profile and relatively little substructure (Fig. 1), but it is thought this disguises a rather eventful dynamical history. Spectroscopic observations reveal two distinct components in the line of sight: a dominant 'cluster' which has a velocity dispersion of ∼1000 km s^{-1}, and a foreground subgroup offset by $\Delta v \sim 3000$ km s^{-1} which has a velocity dispersion of ∼500 km s^{-1} (Fig. 2). The subgroup appears to have undergone a high speed collision with the cluster around ∼3 Gyr ago (Czoske et al. 2001, 2002).

Czoske et al. (2002) explored the proposed cluster – subgroup collision via numerical simulations of dark matter haloes, concluding that this scenario could explain a well-documented discrepancy between mass estimates derived from lensing (e.g. Comerford et al. 2006; Hoekstra 2007; Zitrin et al. 2009; Umetsu et al. 2010), velocity dispersion (Diaferio, Geller & Rines 2005) and X-ray studies (Soucail et al. 2000; Ota et al. 2004; Zhang et al. 2005). Cl 0024 has a lower X-ray flux and lower central velocity dispersion than expected for a virialized system, and this leads to some interesting implications. Processes such as galaxy harassment are usually most effective in the outskirts of clusters, or within groups as a method of 'pre-processing', since the lower relative velocity of galaxies leads to longer interaction times. However Moran et al. (2007) suggest that for Cl 0024, harassment may be effective down to surprisingly small radii, with ram pressure stripping weak until ∼300 kpc from the core. Passive spirals appear to be relatively long lived (1–2 Gyr; Treu et al. 2003) with galaxies experiencing a slower transition due to tidal interactions. In this respect Cl 0024 makes a useful analogue to higher redshift clusters which are still in the process of assembling.

2.2 Target selection

To identify a sample of dust obscured cluster starbursts suitable for VLT/FLAMES IFU observations, we exploit the *Spitzer*/MIPS 24 μm imaging from Geach et al. (2006) and select bright mid-infrared bright sources with 24 μm fluxes of $S_{24\,\mu\rm m} = 0.15$–1 mJy (median $S_{24\,\mu\rm m} = 0.33 \pm 0.03$ mJy) which have also been spectroscopically confirmed as cluster members (Moran et al. 2005). Approximately two-thirds of the sample are known Hα or [O II] emitters, as identified from Suprime-Cam narrow-band Hα imaging and DEIMOS spectroscopy (Kodama et al. 2004; Moran et al. 2005). We also include two Hα emitters of unknown 24 μm flux (IDs 9 and 10) which we used to fill vacant IFUs. We find no further distinction between these two galaxies and the rest of the sample,

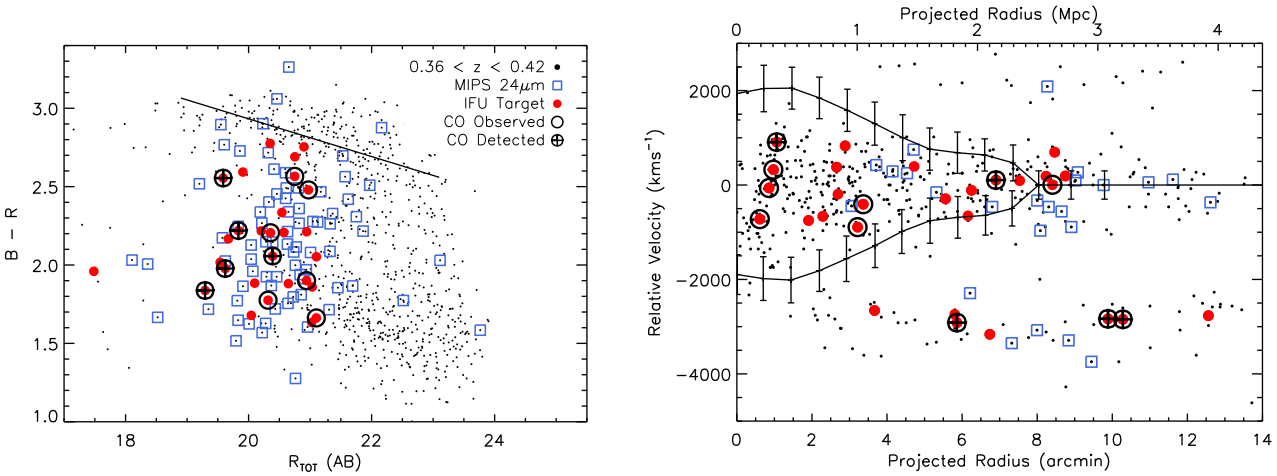

Figure 2. Properties of our starburst sample. Left: colour–magnitude relation for galaxies within a 9 arcmin radius of the Cl 0024+17 cluster centre and within $\Delta z < 0.03$ of the cluster redshift. We identify the cluster red sequence (solid line). Many targets in our sample lie between the red sequence and blue cloud – a consequence of dust-obscured star formation in blue, star-forming galaxies. Right: line-of-sight velocity with respect to the cluster centre, versus projected cluster-centric radius. Solid lines show the caustics which illustrate the escape velocity of the cluster (Diaferio et al. 2005). The structure at ∼−3000 km s^{-1} appears to be a group in the line of sight, which previously passed through Cl 0024+17 (Czoske et al. 2002). Seven of our cluster starbursts lie within this foreground structure.

suggesting they are cluster starbursts which are simply not as dust obscured.

As shown by Figs 1 and 2, our final starburst sample of 28 galaxies is well dispersed throughout the cluster, with projected cluster-centric radii of $R = 0.2$–3.9 Mpc. 20 of 28 galaxies lie within the cluster virial radius of $R_{\rm vir} = 1.7$ Mpc (Treu et al. 2003). Seven of our targets are associated with the foreground group, which will allow us to assess the effect of an accelerated environment on the galaxy properties.

In Fig. 2, we show the $(B-R)$ colour for all galaxies within the redshift range $0.36 \leq z \leq 0.42$ (equivalent to $\Delta v \sim 9000$ km s^{-1}). No colour cut was made in selecting our IFU sample, and as can be seen from this figure, the MIPS 24 μm detections and our IFU targets tend to lie either in the blue-cloud or between the blue-cloud and the cluster red sequence (which can be identified between $(B-R) \sim 2.5$–3.2). Some starbursts likely show redder colours due to the influence of dust on a population of intrinsically blue and star-forming galaxies.

In our analysis, we also exploit archival observations of Cl 0024+17 which were taken with *HST*/WFPC2 as a 39-point sparse mosaic (Treu et al. 2003). The images were taken with the *F*814*W* filter (corresponding to rest-frame 580 nm) and cover approximately one-third of our sample (Fig. A1). We find a high incidence of discs with a range of bulge to disc ratios, and none of the galaxies appear to be undergoing a major merger. We note that there is no obvious trend in morphology with projected cluster-centric radius or association with the cluster or foreground group.

2.3 FLAMES IFU observations

Observations of our 28 starbursts were made using the FLAMES multi-object IFU system on the VLT between 2012 December 13 and 2013 November 29 as part of ESO runs 089.A-0983 and 092.A-0135. FLAMES employs 15 IFUs across a patrol field of 25 arcmin diameter (Fig. 1) and each of the deployable integral field units consists of a near rectangular array of 20 microlenses (with pixel scale 0.52 arcsec × 0.52 arcsec), resulting in a total aperture of ∼3 arcsec × 2 arcsec. All of the observations were taken in dark time and excellent seeing (<0.5 arcsec). We used the GIRAFFE spectrograph with the LR 881.7 filter to cover the Hα emission line in all of our targets, which at $z \sim 0.39$ is redshifted to ∼9100 Å. At this wavelength the spectral resolution is $R = \lambda / \Delta\lambda \sim 9000$ (as measured from skylines), and we correct for this instrumental dispersion in all of our observations. Each observing block was split in to two 1.2 ks observations, with subpixel dithers to improve the effective spatial sampling. The total on-source integration time per target was 3–4 h.

To reduce the data we used the standard ESOREX pipeline, which extracts the fibres from each IFU, flat-fields and wavelength calibrates to form a set of preliminary data cubes. We reduced each observation individually, before sky subtracting and flux calibrating the spectra. For sky spectra, we masked emission lines and continuum from the IFUs and then calculated an average sky spectrum which was then removed from all targets.

To create a mosaic for each galaxy we apply the subpixel offsets from our dither patterns, which were verified using the centroided continuum emission from the three brightest galaxies in the sample. This resulted in an effective pixel scale of 0.17 arcsec. In combining the data cubes we used a 3σ clipped average. The final spectra, integrated over each IFU, are shown in Appendix A along with the *HST* (where available; Treu et al. 2003) or Subaru imaging (Kodama et al. 2004). All but one of the targets were detected (and spatially resolved), leaving us with a final sample of 27 cluster starbursts. We note that the undetected target was the galaxy with the weakest Hα emission in the parent catalogue. We exclude this source from the rest of the analysis.

To create the two-dimensional Hα emission, velocity and velocity dispersion maps, we first measure the systemic redshift by fitting the Hα and [N II]$\lambda\lambda$6548, 6583 emission lines in the collapsed spectra. We then repeat this procedure on a pixel-by-pixel basis using a χ^2 minimization procedure, inverse weighting the fit using a sky spectrum to account for increased noise at the positions of OH sky lines. We fit the Hα and [N II] doublet emission lines simultaneously, allowing the centroid, intensity and width of the Gaussian profile to vary. The full width at half-maximum of the Hα and [N II] lines are coupled and the intensity ratio of the [N II] λ6548/λ6583 was fixed at 2.98. We require an SNR > 5 in order to record a detection in each individual pixel. During the fitting, we convolve the line profile with the instrumental dispersion. As such, all measurements are corrected for the instrumental resolution.

Fig. 6 shows the Hα velocity field of each of our sample, and in Fig. A1 we show the resolved Hα emission, dynamics and line-of-sight velocity dispersion maps of all galaxies. Although we observe a range of Hα morphologies, the majority of the sample appear to have regular (disc-like) velocity fields with velocity dispersions which peak towards the dynamical centre. It is useful to note that in the galaxy integrated one-dimensional spectra (Fig. A2), more than half show emission lines profiles which are double peaked. This is also indicative of disc-like dynamics, with either increased dust obscuration towards central regions, or ring-like emission. We will return to a more detailed discussion of the dynamics in Section 4.

2.4 Plateau de Bure observations

To assess the evolutionary state of our target galaxies, we have also sought to obtain cold gas masses for a subset. This will allow us to compare the gas properties to field galaxies of a similar mass at the same redshift. We used the IRAM PdBI and its NOEMA upgrade to target the ^{12}CO $J(1 \rightarrow 0)$ transition in 11 galaxies, five of which were previously presented in Geach et al. (2009, 2011). These initial targets were predominantly in the outskirts of Cl 0024+17, with cluster-centric radii of 1.8–3.3 Mpc, and so to complement this data we selected a further six galaxies which lie closer to the (projected) cluster core (Fig. 1). Observations took place in 2014 June as part of programme S14BT. Both sets of observations analysed here used the compact 'D' configuration using six or seven antennas. We targeted the ^{12}CO $J(1 \rightarrow 0)$ 115.27 GHz rotational transition, which $z = 0.395$ is redshifted into the 3 mm band with $\nu_{\rm obs} = 82.63$ GHz. The central frequency of the 3 mm receiver was set to coincide with the CO(1−0) line at the spectroscopic redshift. For further details on the setup of the first set of observations, see Geach et al. (2011).

For the most recent sample, since one frequency setup was sufficient to cover all targets we required only one phase calibrator, switching between three pointings. The correlator was set up with 2.5 MHz spacing (2 × 64 channels, 320 MHz bandwidth), so as to accommodate any potential offset from the systemic redshift or a broad emission line profile. To increase observing efficiency, we chose pointings where two cluster starbursts had sufficiently small on-sky separations that they lay within a single primary beam. Exposure times were 4.15 h per source pair. The data were calibrated, mapped and analysed using the software GILDAS (Guilloteau & Lucas 2000).

Combining our six new observations with those from Geach et al. (2011), we detect the CO $J(1 \rightarrow 0)$ transition in five of

11 targets. We require 3σ for a detection, with upper limits on $L'_{\rm CO}$ for non-detections based on the rms noise and median line width of the sample. One-dimensional spectra are shown in appendix Fig. A2. For the five detections, we find line fluxes in the range $f_{\rm CO(1\text{-}0)} = (255\text{–}788)$ mJy km s^{-1} and an average line width of $\sigma_{\rm CO} = 140 \pm 25$ km s^{-1}. To estimate the average flux of the sample we stack the CO spectra from all 11 galaxies. We find $f_{\rm CO(1\text{-}0)} = 309 \pm 30$ mJy km s^{-1}, and derive the same flux independent of whether we take an average, a median, or a noise weighted sum. Despite only one new detection, stacking the data allows us to place important constraints on the gas properties of these starbursts. We will return to this in Section 3.

3 ANALYSIS AND DISCUSSION: GALAXY INTEGRATED PROPERTIES

Before discussing the dynamics, star formation and molecular gas properties of our cluster starburst sample, we first derive their stellar masses and SFR using the multiwavelength imaging available for the cluster. This allows the properties (current and final stellar mass, baryon fraction, dynamical state, gas depletion time-scale) to be set in context with the field and cluster population at the same redshift.

3.1 Stellar masses

We begin by deriving absolute *K*-band magnitudes and stellar masses for the galaxies in our sample, using eight-band photometry from the optical to mid-infrared. The *BVRI*-band fluxes were taken from Czoske et al. (2002) and Treu et al. (2003) (which comprises Canada–France–Hawaii Telescope CFHT12k imaging). The *J*- and *K*-band photometry is given in Kneib et al. (2003) and Smith et al. (2005), and is extracted from observations made with the WIRC camera on the Palomar Hale 200 inch telescope. In the mid-infrared, we perform aperture photometry using archival *Spitzer* IRAC imaging in the 3.6 and 4.5 μm bands. In all cases, we use 2.5 arcsec aperture magnitudes and apply the appropriate aperture corrections to total magnitudes.

To fit the spectral energy distributions (SEDs) of each galaxy and hence infer star formation histories and stellar masses, we employ the HYPERZ fitting code (Bolzonella, Miralles & Pelló 2000). Model SEDs are characterized by their star formation history and parametrized by age, reddening and redshift. Using spectral templates derived from the Bruzual & Charlot (2003) evolutionary code, we consider six star formation histories: a single burst (B), constant star formation (Im), and exponential decays of time-scales 3, 5, 15 and 30 Gyr (Sa, b, c, d, respectively). We use the Calzetti et al. (2000) reddening law and, given the obscured nature of these cluster starbursts we allow $A_V = 0.0$–2.5 mag in steps of $A_{\rm V} = 0.1$. We find an average extinction across the sample of $A_V = 1.2 \pm 0.4$ mag. In each case, we fix the redshifts of the synthetic templates to match the Hα emission.

We next integrate the best-fitting star formation history to calculate the stellar mass of each galaxy, accounting for mass-loss from remnants using the STARBURST99 synthesis models (Leitherer et al. 2011). Given the dusty nature of these galaxies, we note that there are degeneracies between age and reddening which results in considerable uncertainty in the stellar mass-to-light ratios, an issue that is likely to be compounded by complex star formation histories. To overcome some of these difficulties, we derive the rest-frame *K*-band mass-to-light ratio a galaxy-by-galaxy basis, and then reapply the average value to the entire sample. The average mass-to-light ratio is $\langle \Upsilon_\star \rangle = {\rm M}_\odot/{\rm L}^K_\odot = 0.35$, and using this technique we find galaxies in our sample to have stellar masses in the range of $M_\star = (1\text{–}10) \times 10^{10}$ M$_\odot$, with a median of $M_\star = (2.8 \pm 0.3) \times 10^{10}$ M$_\odot$. We will use these values in the rest of our analysis. Absolute *K*-band magnitudes and stellar masses (using the median $\Upsilon_\star$) are given in Table A2 of the appendix.

To compare the stellar masses to those of field galaxies at the same redshift, we exploit the COSMOS/UltraVISTA survey from Muzzin et al. (2013), who derive a characteristic mass of $M_\star = (5.8 \pm 0.5) \times 10^{10}$ M$_\odot$ at $z \sim 0.4$. This suggests that, on average, the galaxies in our cluster starburst sample have slightly lower stellar masses than the 'typical' $M_\star$ field galaxy at this redshift.

3.2 Star formation rates

To estimate the SFR of these galaxies we adopt two approaches, using the (reddening corrected) Hα and the far-infrared imaging with *Herschel*. We detect strong Hα emission in the integrated spectra of all but one of our 28 IFU targets (which we have consequently dropped from the sample), with luminosities in the range $L_{{\rm H}\alpha} \sim 10^{40.6\text{–}41.8}$ erg s^{-1} (see Fig. A1 and Table A1). We also make clear detections of the neighbouring [N II]λ6583 line, with ratios of $-0.69 < \log([{\rm N\,II}]/{\rm H}\alpha) < 0.04$ and a median of -0.4 ± 0.02. Since two of our sample exhibit $\log([{\rm N\,II}]/{\rm H}\alpha) > 0$, we discuss the possibility of AGN contamination in Section 4. We note that while the Hα SFR of AGN may be unreliable, the far-infrared results are less likely to suffer contamination.

We use the integrated Hα luminosity to calculate SFR estimates, applying the calibration of Kennicutt (1998) for a Chabrier IMF (SFR M$_\odot$ yr^{-1} $= 4.6 \times 10^{-42}$ L$_{{\rm H}\alpha}$ erg s^{-1}). Using the attenuation, A_V, returned by HYPERZ we also apply the dual reddening law of Wuyts et al. (2013) which assumes that the nebular emission is more attenuated than the stellar continuum (since young, ionizing stars will typically reside in dustier regions). Therefore applying dust corrections of an average $A_{\rm gas} = 1.8 \pm 0.5$ mag, we estimate Hα star formation rates of ${\rm SFR}_{{\rm H}\alpha} = 0.3$,–16 M$_\odot$ yr^{-1}.

To compare far-infrared SFR to those derived from Hα emission, we next exploit the *Herschel* PACS/SPIRE imaging of Cl 0024+17. For PACS, deblended catalogues are available for the cluster core (Lutz et al. 2011), which covers five of the galaxies in our sample. To derive 250, 350 and 500 μm flux densities, we use SPIRE imaging from the HerMES legacy programme (Oliver et al. 2012). We first align the astrometry of the images by stacking at the 24 μm positions, applying <1 arcsec shifts in ΔRA and ΔDec, and then deblend following the procedure of Swinbank et al. (2014), using the *Spitzer* 24 μm sources as priors. From our sample of 27 cluster starbursts, 20 are detected above 11 mJy at 250 μm. The median 250, 350 and 500 μm fluxes for the detections in each band are 20 ± 3, 11 ± 2 and 9 ± 3 mJy, respectively.

To derive far-infrared luminosities we fit the far-infrared flux densities at the spectroscopic redshift, using the far-infrared templates from the Chary & Elbaz (2001), Draine et al. (2007) and Rieke et al. (2009) SED libraries. At the cluster redshift, polycyclic aromatic hydrocarbon (PAH) and silicate features lie bluewards of the 24 μm band, and so we include all photometry between 24 and 500 μm. Integrating the best-fitting SEDs we then derive bolometric luminosities of $L_{\rm IR} = (0.47\text{–}2.47) \times 10^{11}$ L$_\odot$, corresponding to star formation rates of ${\rm SFR}_{\rm IR} = 3$–26 M$_\odot$ yr^{-1}. Far-infrared luminosities and SFR are given in Table A2.

For galaxies with many upper limits on their far-infrared fluxes, we take the Hα SFR and multiply this by the average ${\rm SFR}_{\rm IR}/{\rm SFR}_{{\rm H}\alpha}$ ratio, to estimate ${\rm SFR}_{\rm IR}$. On average, the SFR derived from the far-infrared is a factor of 2.2 ± 0.4 larger than that derived from the

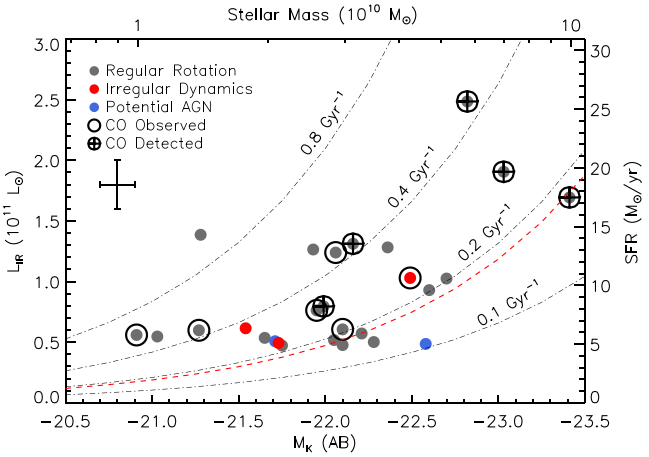

Figure 3. Infrared luminosity against *K*-band absolute magnitude, with additional axes to demonstrate how this relates to SFR and stellar mass. We use the median mass to light ratio for our sample of $M_\odot/L^K_\odot = 0.35$ (see Section 3.1). Dashed lines indicate a constant sSFR, with a red line used to illustrate the sSFR of the so-called main sequence at $z = 0.4$. We highlight galaxies observed using PdBI/NOEMA, and find that detected galaxies tend to be of higher mass and brighter L_{IR}. Red points are used to represent galaxies with dynamics which deviate from a rotating disc model, and blue points for galaxies which may have an AGN affect the dynamics (these classifications are assigned in Section 4). We find no relationship between L_{IR}, M_K and Hα dynamics.

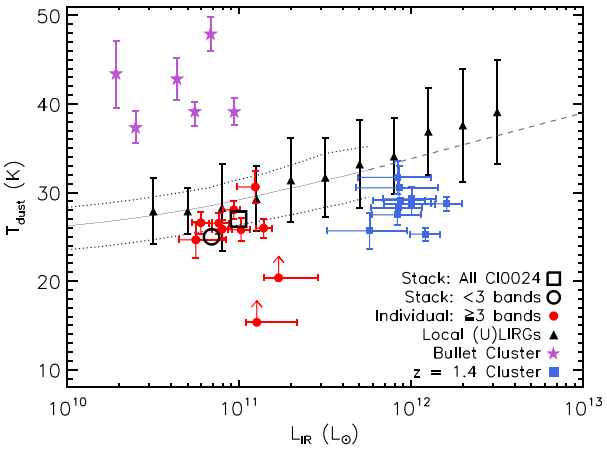

Figure 4. Characteristic dust temperature versus far-infrared luminosity for our cluster starburst sample, compared to the relation established for local starburst galaxies (black triangles show $z < 1$ (U)LIRGs; Symeonidis et al. 2013). Galaxies with detections in three or more infrared bands are shown in red points. We also show stacks of all 27 galaxies (open square) and those with fewer than three detections (open circle). We do not observe a significant offset from the local relation, in either direction. For comparison, we plot the 'hot' Bullet Cluster starbursts of Rawle et al. (2012) which may have been stripped of their low-density gas, and starbursts from a cluster at $z = 1.4$ (which are consistent with high-redshift field galaxies; Ma et al. 2015).

Hα, even after applying a dust correction to the Hα luminosity. This is equivalent to an additional $A_{gas} = 0.9 \pm 0.2$ (or $A_V = 1.3 \pm 0.2$). This offset may arise due to the differing structures between the dust and stars, particularly if the starbursts are centrally concentrated in an otherwise extended disc. Since the SED fitting provides a luminosity weighted result, the attenuation predicted from HYPERZ will be dominated by the extended disc and so systematically low. As a proxy for the SFR, in the rest of our analysis we will use the values derived from the far-infrared fluxes.

In Fig. 3, we plot infrared luminosity versus absolute *K*-band magnitude for the galaxies in our sample, converting the values also to SFR and stellar mass, respectively. We derive specific star formation rates (sSFR) in the range (0.1–0.9) $M_\odot$ Gyr^{-1} with a median of sSFR $= 0.27 \pm 0.03$ Gyr^{-1}. Our cluster galaxies (excluding one AGN candidate, see Section 4) lie on or above the so-called main sequence at $z \sim 0.4$ (Elbaz et al. 2007; Noeske et al. 2007; Karim et al. 2011). On average the galaxies are offset from the main sequence by a factor of 1.8 ± 0.2 at a fixed stellar mass, and hence we adopt the term 'starburst'. In Section 4, we assign each galaxy a dynamical classification – rotationally supported or irregular – based on their velocity map and line-of-sight dispersion map. In Fig. 3, we split the sample by classifications and do not see any strong trends between the SFR and the dynamical state of the galaxy.

3.3 Characteristic dust temperatures

The far-infrared observations also contain information regarding the characteristic dust temperature. Recently, observations of local clusters have revealed a population of apparently 'hot' starbursts, with $T_d \sim 50$ K and LIRG-like luminosities (Rawle et al. 2012). These galaxies may represent a particular stage in the transition from infalling spiral to cluster S0, where ram pressure has stripped the low density (cold) gas disc but a central starburst is yet to be quenched. In order to test whether the cluster starbursts in our sample are more or less evolved, we plot their far-infrared luminosity versus dust temperature in Fig. 4. For consistency with other comparison samples, we employ a modified blackbody curve of the form $S_\nu \propto \nu^\beta B_\nu T_d$ to derive the dust temperatures, with an emissivity index of $\beta = 1.8$. We only include galaxies with detections in three or more bands, which constitutes approximately a third of the sample. This cut means that a reliable estimate of T_d can be derived.

On the plot, we include the relationship for local (ultra) luminous infrared galaxies (LIRGs/ULIRGs) which is derived from a sample of 60 μm selected galaxies at $z \sim 0$ (Chapman et al. 2003; Chapin, Hughes & Aretxaga 2009) and SPIRE-selected $z < 1$ (U)LIRGs (Symeonidis et al. 2013), both of which follow a power-law relation between $L_{IR} \sim 10^{10}$–10^{13} $L_\odot$. We also plot similar measurements of high-z submillimetre-selected cluster starburst galaxies in XCS J2215.9−1738 ($z = 1.4$), which show systematically colder dust temperatures at fixed luminosity compared to the local relation (Ma et al. 2015). This is likely to be a result of the more extended gas reservoirs compared to $z = 0$ galaxies of the same luminosity.

For our sample of cluster starbursts, we derive a median dust temperature of $T_d = 26 \pm 1$ K and far-infrared luminosity $L_{IR} = (9.1 \pm 0.9) \times 10^{10}$ $L_\odot$. These dust temperatures are consistent with those measured for low-redshift field galaxies of similar far-infrared luminosity, and indeed we do not find any starburst galaxies with dust temperatures exceeding 31 K. However, we note that in this analysis we have only included the galaxies with detections in three (or more) bands, and for two of these galaxies we place lower limits on T_d since we do not resolve the peak of the emission. To infer the average dust temperature of the remaining sample we stack the PACS and SPIRE images in four different ways: all 27 galaxies, galaxies detected in ≤1 band, in ≤2 bands and in <3 bands. The characteristic dust temperatures of these subsets are all within 2 K of each other (25–27 K), suggesting that the galaxies with well-defined blackbody fits are representative of the full sample. We plot the temperatures of the full sample stack and the <3 bands stack in Fig. 4 for comparison.

Finally, we note that although we only selected a small subsample for IFU follow-up, the 24 μm MIPS parent sample comprises 60 galaxies in total, approximately one-third of which lie in the foreground group. To search for differences between the group and cluster starbursts, we stacked the PACS and SPIRE imaging of the 24 μm-detected galaxies in both subsets, but in each case the SPIRE colours and characteristic dust profiles are consistent, with $T_{\rm d,\,cluster} = 23 \pm 2$ K and $T_{\rm d,\,group} = 23 \pm 3$ K, respectively.

Thus, it appears that the characteristic dust temperatures of cluster starbursts are consistent with a luminosity matched sample of field galaxies. In this respect, our sample appear to be less evolved than the 'hot' starbursts seen in some local clusters (Rawle et al. 2012), perhaps indicating that they have been accreted more recently, and have not yet had their low-density gas stripped by the ICM.

3.4 Molecular gas masses

To determine how the molecular gas content of these galaxies compares to similar mass field galaxies, and calculate their likely final stellar mass if all available gas is converted to stars, we use the ^{12}CO $J(1 \rightarrow 0)$ emission. We overlay the CO spectra on top of the Hα in Fig. A2, and find that the velocity centroid and line widths are well matched. The two sets of spectra have an average velocity offset of 50 ± 10 km s^{-1}, and an average ratio between the Hα and CO line widths of 0.9 ± 0.2. This suggests that the ^{12}CO traces the same dynamics as the Hα emission, and that the ionized gas and molecular gas components are similarly distributed throughout the disc.

Fitting each of these ^{12}CO spectra with a single Gaussian profile, we find line luminosities of $L'_{\rm CO} = (2.2\text{–}6.8) \times 10^9$ K km s^{-1} pc^2 for the five detected galaxies (Solomon & Vanden Bout 2005), and upper limits of $L'_{\rm CO} = (3.9\text{–}4.9) \times 10^9$ K km s^{-1} pc^2 for the rest of the sample (see Table A2). To convert to the molecular gas mass we use $M({\rm H_2 + He}) = \alpha\, L'_{\rm CO}$. The far-infrared luminosities of our targets are much larger than what is typical of local star-forming galaxies such as the Milky Way (Gao & Solomon 2004), however as discussed in Geach et al. (2011) the choice of $\alpha = 4.6$ may be the most appropriate given the late-type morphologies of the sample, and that the average $L_{\rm IR}/L'_{\rm CO}$ ratio we measure ($L_{\rm IR}/L'_{\rm CO} = 25 \pm 5$) is comparable to local spirals. Using this calibration we estimate molecular gas masses of $M_{\rm gas} = (1.0\text{–}3.0) \times 10^{10}$ M$_\odot$ which equates to gas fractions of $f_{\rm gas} = M_{\rm gas}/(M_{\rm gas} + M_\star) = 0.11\text{–}0.39$. As discussed in Section 2.4, we also stacked all 11 CO spectra to better characterize the sample as a whole. Using this stack we find a median line luminosity $L'_{\rm CO} = (2.7 \pm 0.3) \times 10^9$ K km s^{-1} pc^2, which translates to a gas mass of $M_{\rm gas} = (1.2 \pm 0.2) \times 10^{10}$ M$_\odot$ (towards the lower end of our detections). We will use this as a representative gas mass for our sample in all of the analysis below.

Our CO sample have an average SFR of (13 ± 1) M$_\odot$ yr^{-1} (compared to $\sim$10 M$_\odot$ yr^{-1} for the wider sample) and so we estimate a gas depletion time-scale of $\sim$1 Gyr, which is approximately $\sim$0.25 of the cluster crossing time. This may explain the non-detections of the ^{12}CO in the (projected) cluster core. We predict final stellar masses for our sample with an average of $\sim 4 \times 10^{10}$ M$_\odot$. From a sample of local cluster S0s ($0.04 < z < 0.07$; WINGs survey), Vulcani et al. (2011) find a characteristic stellar mass of $M_* = 2.2 \times 10^{11}$ M$_\odot$. This implies that our cluster starbursts are destined to be $\leq M_*$ members of the S0 population. It may be that the most massive $\leq M_*$ S0s are already in place at this redshift, or that their progenitors are passive spiral galaxies which have already completed their starburst phase.

As shown in Fig. 2, our ^{12}CO sample includes galaxies of range of cluster-centric radii, and which inhabit both the 'main' cluster and subgroup component. While all three galaxies observed in the subgroup are detected in ^{12}CO, only two of eight galaxies are detected in the larger structure. This could be an environmental trend. However, we also caution that the galaxies which we detect also tend to be more far-infrared luminous, and given the correlation between $L_{\rm IR}$ and $L'_{\rm CO}$, this may simply mean the ^{12}CO is easier to detect. Of course we cannot rule out the possibility that the same sources are brighter in the far-infrared due to some evolutionary effect. Considering our limited sample size, it is difficult to draw definitive conclusions with respect to the gas content as a function of cluster radius, but this study motivates a more detailed future study with a larger sample.

To compare the gas masses of these starbursts to galaxies on the star-forming 'main sequence' at this redshift, we use the scaling relations of Genzel et al. (2015). These relations predict that a star-forming galaxy at $z \sim 0.4$ with a similar stellar mass will have a gas-to-stellar ratio of $\log(M_{\rm gas}/M_\star) \sim -0.9$. This implies an average gas mass of $M_{\rm gas} \sim 4\text{–}8 \times 10^9$ M$_\odot$. The molecular gas masses of our sample therefore appear to be slightly higher (a factor of $\sim$2) than those of 'typical' galaxies of similar stellar mass at this redshift. The far-infrared and CO luminosities of our sample are consistent with the $L_{\rm IR}$–$L'_{\rm CO}$ relation fit to low- and high-redshift star-forming galaxies (including LIRGs, ULIRGs and SMGs) in Ivison et al. (2013).

Finally, we compare the gas properties of our cluster starbursts to starbursts in the field population, using a sample of ULIRGs ($L_{\rm IR} > 10^{12}$ L$_\odot$) at $0.2 < z < 1$ taken from Combes et al. (2013). This comparison sample have SFR $\sim$10$\times$ higher than our cluster starbursts, but by mass matching their sample to the median stellar mass of our galaxy sample, we derive an average gas mass of $M_{\rm gas} = (1.2 \pm 0.5) \times 10^{10}$ M$_\odot$. This is consistent with the molecular gas masses derived for our cluster starburst sample.

On the basis of our ^{12}CO observations, it appears that these cluster starburst galaxies are richer in molecular gas than typical star-forming galaxies at a similar redshift. We derive molecular gas masses which are more closely matched to those of starbursts (ULIRGs) in the field with similar infrared luminosities. This could suggest a scenario in which the gas of infalling galaxies is compressed upon their encounter with the ICM, converting available H I into H_2 and triggering a burst of star formation. These galaxies may have been typical star-forming galaxies upon accretion to the cluster, yet have their molecular gas fraction enhanced through this process. We will return to these results in the final section.

4 ANALYSIS AND DISCUSSION: IONIZED GAS DYNAMICS

4.1 Disc fitting

Now that we have established the integrated properties of our sample, we next investigate the spatially resolved properties as measured from the Hα emission. The galaxies in our sample appear to resemble the field population in terms of their stellar masses and characteristic dust temperatures (although possibly with higher molecular gas masses), and so our aim in this section is to assess how evolved these galaxies appear in terms of their gas dynamics. We will search for evidence of the mechanisms which may eventually quench the star formation in these galaxies and transform their

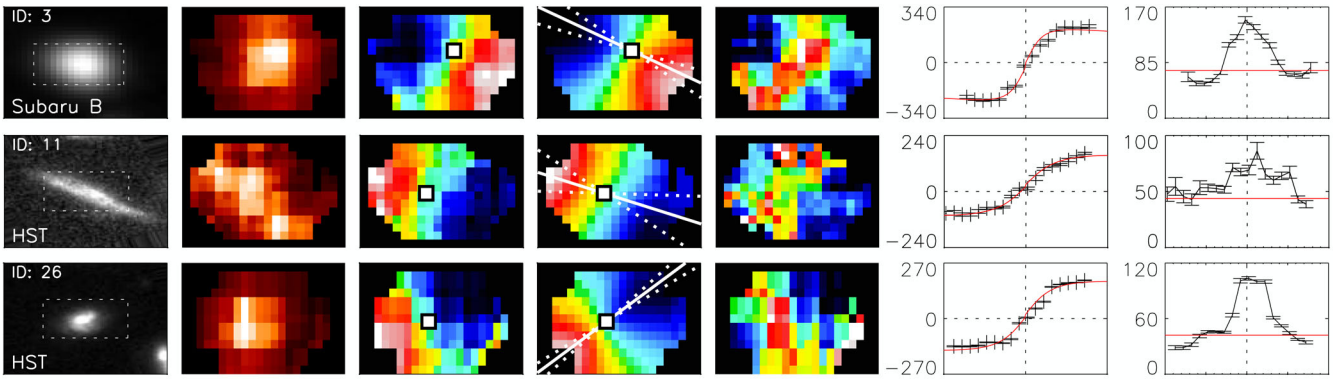

Figure 5. Example broad-band image, Hα morphology and dynamics for three galaxies in our sample (data for the complete sample is shown in Fig. A1). From left to right: Subaru or *HST* broad-band image, Hα intensity map, Hα velocity field, best-fitting model velocity field, dispersion map and the rotation curve and line-of-sight velocity dispersion profile extracted along the primary axis. The dashed outline on the broad-band image illustrates the position and size of the IFU (2 arcsec × 3 arcsec). We fit the two-dimensional data using a simple inclined disc model. The solid line placed on to the model velocity field shows the position angle, and the dashed lines reflect the 1σ uncertainty of this. The square points indicate the position of the dynamical centre, according to the best-fitting model. We fit the one-dimensional rotation curve (in red) to find a characteristic rotation velocity. Axes are in units of km s^{-1}. The solid red line in the last plot shows the value of σ_0. We find ∼90 per cent of our starburst sample resemble undisturbed rotating discs, with a characteristic 'spider' pattern in the velocity field, and a line-of-sight velocity dispersion which peaks towards the dynamical centre.

kinematics from regular, disc-like rotation to pressure-supported S0s.

In Fig. A1 we show the two-dimensional maps of Hα emission, velocity and line-of-sight velocity dispersion for all 27 targets. In each instance there is a clear velocity gradient with peak-to-peak differences ranging from $\Delta v = 100$ to 500 km s^{-1}. We note two galaxies (IDs 23 and 24) exhibit very high log ([N II]/Hα) ratios (i.e. $\gtrsim$0); indicating the presence of an AGN (e.g. Kewley et al. 2013). Additionally, these sources show irregular velocity dispersion profiles, with spatially offset broad emission ($\gtrsim$150 km s^{-1}; Fig. A1), which may indicate that outflows are affecting the gas kinematics in these sources (e.g. Harrison et al. 2016). For these reasons, we omit these two galaxies from the dynamical analysis below, leaving a sample of 25.

Next, we assign a dynamical classification to each of the galaxies in our sample(Fig. 3; Table A3). We classify 22 of 25 starbursts (∼90 per cent) as rotationally supported, since their velocity map is regular (with a characteristic 'spider' pattern), their rotation curve smooth, and they possess a line-of-sight velocity dispersion map which peaks towards the dynamical centre. The optical morphologies of these galaxies also appear smooth (and in some cases disc-like), with no evidence of multiple centres, tidal tails or merger activity. We class the remaining three galaxies as irregular, since they show complex dynamics in their two-dimensional maps, rotation curves or dispersion profiles. This fraction of discs is consistent with field surveys at these redshifts, which have suggested that massive galaxies are the most well ordered at all redshifts up to $z \sim 1.5$ (e.g. Kassin et al. 2012; Wisnioski et al. 2015; Stott et al. 2016, but see also Puech et al. 2007). In Fig. 3, we demonstrate that the kinematics do not appear to be correlated with far-infrared luminosity or *K*-band magnitude.

To provide a quantitative measure of the dynamics, and derive their basic parameters (such as disc inclination, i and hence true rotational speed), we fit each velocity field using a simple disc model with arctan rotation curve (e.g. Courteau 1997). In total we fit for six different parameters: the dynamical centre (x_c, y_c), asymptotic velocity v_c, velocity at centre of rotation v_0, turnover radius r_t, position angle θ and disc inclination i. Although all velocity fields show small discrepancies the majority appear to be well fit by this simple model, with $\langle v_{\rm data} - v_{\rm model} \rangle = 26 \pm 15$ km s^{-1}. Example dynamical maps are shown in Fig. 5, and similar images for the full sample are given in appendix Fig. A1. We note that the position angle and dynamical centre returned by the model fit clearly pass through the regions of minimum and maximum rotation velocity. We also compare our inclination values to those derived from the *HST* and Subaru optical morphologies. Although there is some degree of scatter, we find our conclusions in the following sections would be unchanged had we used inclinations derived directly from the images instead. Where the inclination of a particular galaxy is more uncertain, this is reflected in the larger errors assigned to dynamical parameters in Table A3.

Using the best-fitting disc parameters, we extract one-dimensional rotation curves by collapsing the velocity field along the major kinematic axis. It is clear from these data that a number of the rotation curves asymptote and turn over beyond ∼2 kpc. To fully characterize this shape, we fit the rotation curves with a model that includes a dark matter component. The velocity field can therefore be expressed as $v^2 = v_{\rm d}^2 + v_{\rm h}^2 + v_{\rm HI}^2$, where the subscripts denote the stellar disc, dark matter halo and H I gas disc, respectively. For the stellar disc, we assume the stars follow an exponential surface density (Freeman 1970) which is characterized by a disc mass and radius, and for the dark matter we assume $v_{\rm h}^2(r) = G\,M_{\rm h}(< r)\,/\,r$, with a dark matter density profile that is described by a core density and radius. Further details of the modelling used are discussed in Swinbank et al. (in preparation). Although we do not attempt to infer the stellar/dark halo fractions (due to strong degeneracies), this parametrization allows us to improve our measurement of total rotation speed at the disc radius. While in most cases we could extract this velocity directly from the raw data, a model is useful for when this is not possible. In the following analysis, we use inclinations from the two-dimensional disc model and rotation velocities from this one-dimensional rotation curve fit.

As a representative rotation velocity we choose to define $v_{2.2}$, the velocity at 2.2 × the half-light radius, since this typically samples the rotation curve in a region where it is no longer rising steeply. Of our IFU sample, 10 are covered by deep *HST* imaging and the remaining 17 by Subaru (see Fig. A1), and we use these images to establish the continuum half-light radius ($r_{1/2}$) by fitting a series of

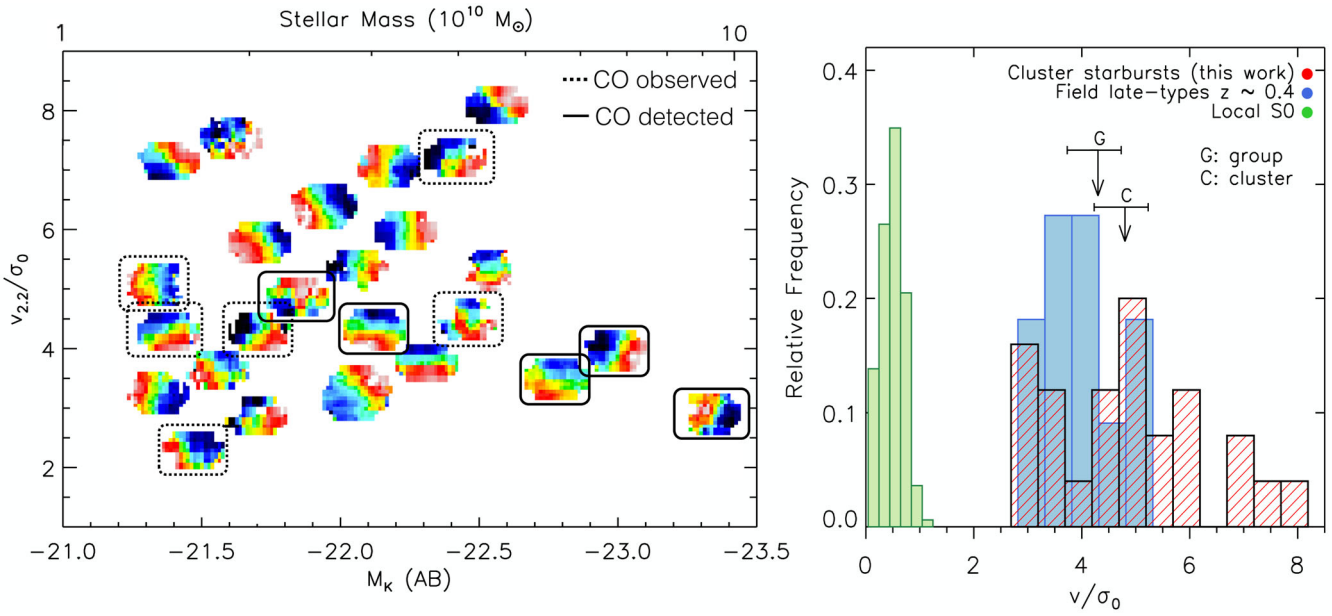

Figure 6. Left: Hα dynamics of the 25 galaxies as a function of rotational support ($v_{2.2}/\sigma_0$) and *K*-band magnitude. We choose to define the characteristic rotation velocity at 2.2 × the half-light radius, as measured from *HST* and Subaru continuum images. We convert M_K values to stellar masses, using the average mass-to-light ratio derived from the HYPERZ SED fitting (see Section 3.1). We circle galaxies for which we have observed the ^{12}CO transition, with solid lines corresponding to $>5\sigma$ detections, and dashed lines elsewhere. Some velocity fields have been shifted a small distance from their original position for clarity; however, these values are provided in Tables A2 and A3. The majority of galaxies resemble undisturbed, rotating discs, with no obvious trends between dynamics and galaxy mass or molecular gas content. Right: the rotational support of our galaxies compared to local S0s (Emsellem et al. 2011) and field spirals of a similar redshift (Puech et al. 2007). The fact that their v/σ_0 values are consistent with field spirals suggests that these galaxies have only recently been accreted. Their discs must be dynamically heated to decrease their v/σ_0 values to match S0s. The median v/σ_0 of the group does not appear to be significantly different to that of the 'main' cluster ('G' arrow and 'C' arrow, respectively).

ellipses at the galaxy position angle. We deconvolve for the seeing, and use the model rotation curve to estimate the velocity at this radius. We give this rotation speed and the corresponding half-light radius in Table A3.

4.2 Turbulence and rotational support

To continue to address the question of which physical mechanism(s) drives the star formation in cluster starbursts, we next measure the turbulence in the ISM. By comparing to galaxies in the field with a mass and SFR matched sample, this will allow us to quantify the effect of environment on the stability of the disc. To calculate the intrinsic velocity dispersion, σ_0, we first correct for beam-smearing effects using the raw two-dimensional velocity field. For each pixel we consider all neighbouring pixels within the point spread function (PSF), and calculate the maximum velocity gradient across this element $\Delta v/\Delta R$. This contribution to the dispersion is then removed and we calculate the average velocity dispersion across the entire galaxy image (inverse weighting by the noise at each pixel). The final corrected velocity dispersions, σ_0, for each galaxy are given in Table A3 and their values also shown relative to the dispersion profiles in Fig. A1. It can be seen that these σ_0 values are comparable to the velocity dispersion in the outer regions of the disc, which is less affected by beam smearing.

We find our cluster starbursts to have a median velocity dispersion of $\sigma_0 = 50 \pm 15$ km s^{-1}. Dynamical studies between $0.2 < z < 1.0$ report values in the range $\sigma_0 = 25$–60 km s^{-1} (e.g. Kassin et al. 2012; Wisnioski et al. 2015; Stott et al. 2016); however, it is difficult to make direct comparisons since estimates are highly sensitive to the properties of the sample and the method used (see Stott et al. 2016 for further discussion). To derive σ_0 in a consistent way and compare to the turbulence of field galaxies at similar redshift, we exploit the sample of Swinbank et al. (in preparation). This sample consists of ∼500 [O II] emitters serendipitously identified in a series of commissioning and science verification observations using MUSE. There were 16 'extragalactic' fields observed, with the science targets largely 'blank' fields or studies of high-redshift ($z > 4$) galaxies and quasars. We match the redshift, stellar mass and SFR of this star-forming sample to our cluster starbursts and find a median of $\sigma_0 = 50 \pm 10$ km s^{-1}. This suggests that turbulence in the gas discs of our galaxies has not yet been enhanced by the various physical processes acting in this dense environment.

The ratio between inclination corrected rotation velocity and intrinsic velocity dispersion, v/σ_0, is often used as a measure of rotational support against thermal pressure. We therefore calculate this parameter for each galaxy in order to compare their dynamics to the field population and cluster S0s, using the characteristic rotation velocities ($v_{2.2}$) calculated in Section 4.1. Across our sample we find inclination corrected values between $v_{2.2}/\sigma_0 = 2.8$ and 8.2, with a median of $v_{2.2}/\sigma_0 = 5 \pm 2$. Given that $v/\sigma_0 < 1$ is typically used as a cut-off for the classification of 'dispersion dominated' galaxies, this further supports our conclusions that the majority of our sample are undisturbed, rotating discs.

In Fig. 6, we compare the rotation of the dusty starbursts to local S0s and spiral galaxies in low-density environments at similar redshift. We plot the v/σ_0 values of 32 rotationally supported galaxies at $0.4 \leq z \leq 0.75$ (also observed using FLAMES). Puech et al. (2007) find a median $v/\sigma_0 = 3.8 \pm 2$, which is consistent with our sample. We also see that local S0s (Emsellem et al. 2011) typically have values of $v/\sigma_0 \leq 1$. The dynamics of infalling cluster galaxies must evolve significantly if a transformation is to take place between spirals and S0s.

Finally, to search for trends in the dynamics as a function of cluster-centric radius, we divide the sample into galaxies within the (projected) cluster core, in the outskirts, and in the foreground subgroup. However, we do not find any link between whether a galaxy resides in one of these regions and its dynamics (in terms of the observed dynamical state, σ_0 or v/σ_0). We show the median v/σ_0 of these two subsamples in Fig. 6. The kinematics also do not appear to be strongly correlated with galaxy mass or SFR (see Fig. 3). Although our results may be complicated by projection effects, it appears that the dynamics of the galaxies are not a strong function of location within the cluster. This implies that any dynamical transformation must take place over a longer period than the duration of the starburst ($\sim$ 1 Gyr), or once the starburst has been quenched.

4.3 Specific angular momentum

Although the ratio of v/σ_0 is a useful measure of the dynamical state of a galaxy, a better quantification is the spin, λ_R, since this encodes how the rotational speed and line-of-sight velocity dispersion vary with radius. Dynamical studies of local galaxies have shown that early-type and late-type galaxies tend to (broadly speaking) have different spin values (Fogarty et al. 2015; Querejeta et al. 2015). Emsellem et al. (2011) define λ_R, which is essentially a proxy for specific angular momentum, as

$$\lambda_R = \frac{\sum_{i=1}^{N} F_i R_i |V_i|}{\sum_{i=1}^{N} F_i R_i \sqrt{V_i^2 + \sigma_i^2}}, \quad (1)$$

where F_i, V_i, σ_i and R_i are the flux, velocity, velocity dispersion and radius of the ith pixel, respectively. This spin parameter was initially used in the classification of early-type galaxies, with Cappellari et al. (2011) finding ellipticals and S0s could be split into two regimes – fast rotators and slow rotators – depending on their spin and ellipticity. However, more recently the spin has been combined with the concentration of the stellar light profile, as a diagnostic tool to test how galaxies might dynamically evolve from one type to another. Concentration, c, is defined as the ratio between the radii enclosing 90 and 50 per cent of the Petrosian flux.

In Fig. 7, we compare the spin and concentration of our sample to the properties of spirals and S0s from the CALIFA survey ($z \sim 0$; Querejeta et al. 2015). For consistency with the comparison samples we evaluate λ_R for all pixels within the half-light radius, deriving a median $\lambda_R = 0.83 \pm 0.06$ and concentration of $c = 2.1 \pm 0.3$ for the cluster galaxies. For this analysis we use *HST* images (*F*814*W* filter) where available, and Subaru z-band images otherwise. As Fig. 7 shows, the dynamics and concentration of our galaxies are consistent with field spirals, implying that the dynamics of our sample are still relatively unaffected by the cluster environment. If these galaxies are to eventually transition to S0s they clearly must undergo a process (or several) which not only dynamically heats the disc and reduces rotational support, but which also increases the bulge to disc ratio (and hence increases the concentration by a factor of $\sim$2).

Interactions with the dense ICM can effectively strip the gas discs of spirals and lead to a rapid truncation of star formation. It was recently suggested that ram pressure stripping may even cause a temporary enhancement of star formation in central regions (Bekki & Couch 2011; Bekki 2014). However, the same numerical simulations predict little effect on the dynamics of these galaxies due to interaction with the ICM. Conversely, tidal interactions are very efficient at disrupting the disc. Repeat galaxy–galaxy encounters can act to increase the velocity dispersion and decrease the spin, potentially

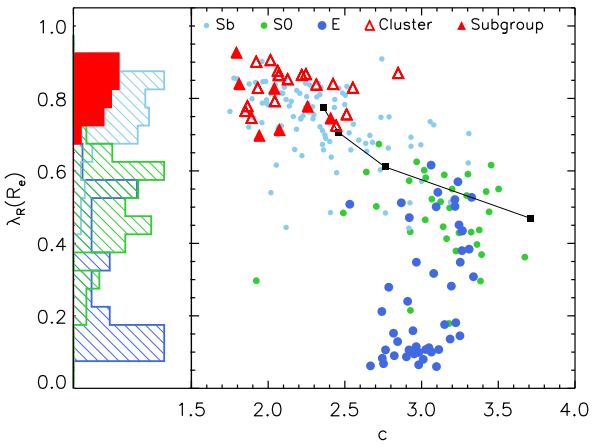

Figure 7. Galaxy spin, λ_R versus concentration, c for our starburst sample, as compared to galaxies of various morphological types from the CALIFA survey (Querejeta et al. 2015). We also overlay predictions from the numerical models of Bekki & Couch (2011), who simulate the impact of tidal interactions on a typical spiral galaxy in a dense environment. Squares along the tracks represent 0, 2.8, 4.2 and 5.6 Gyr since the beginning of this simulation. The high spin values of our galaxies suggest kinematics that are consistent with recently accreted field spirals. It seems that the mechanism which initiated the current burst of star formation has not had a dramatic effect on the disc dynamics. In order to make a transition between spirals and S0s these galaxies must lose angular momentum and increase their bulge to disc ratio (and therefore concentration).

channelling gas inwards to fuel episodes of bursty star formation. Indeed, Bekki (2014) predict that a high spin, low concentration late-type galaxy in a high-mass group may be transformed via tidal interactions into a low-spin, high-concentration S0, over a period of 2–4 Gyr. We overlay this evolution in Fig. 7. Although the timescales likely increase in a cluster environment, such a mechanism would simultaneously achieve the two key changes required for a spiral to S0 transition. In this scenario, the concentration is increased gradually via multiple bursts of star formation in the central regions, and we may expect to find starbursts with a range of λ_R and c values. However, our cluster starburst sample are exclusively high-spin, low-concentration galaxies. We propose instead that the initial encounter with the ICM is responsible for triggering the starbursts observed in this cluster. Repeat galaxy–galaxy interactions may occur after the bursts have been quenched, to eventually achieve the $\sim$40 per cent decrease in angular momentum.

4.4 The beginning of the end?

Overall, the characteristic temperatures, gas masses and dynamics of these dusty starburst galaxies suggest that they have only recently been accreted from the field. The far-infrared SFR are on average twice that of a typical star-forming galaxy at this redshift, with our ^{12}CO observations suggesting that there is sufficient cold gas to sustain this activity for another $\sim$1 Gyr. In fact we calculate molecular gas masses consistent with local ULIRGs. Dust temperatures in line with the local relation are further evidence that the gas discs have not yet been stripped by the ICM.

The dynamics and morphologies of the cluster galaxies appear disc-like, with a large degree of rotational support (v/σ_0) and a high angular momentum (λ_R). There is no evidence to suggest that the current bursts of star formation were initiated by mergers. It is possible that they were instead triggered by ram pressure, as an initial encounter with the ICM compresses the ISM of the infalling

galaxies. This could also convert available H I into molecular H_2, and may explain why these galaxies are so rich in star-forming gas. Such a process is consistent with the small excess of starbursts seen inside the virial radii of some clusters (e.g. Hogg et al. 2006).

As we have seen in Fig. 7, in order for the cluster starbursts to transition from spirals to S0s they must increase their concentration (c) and decrease their angular momentum (λ_R). Multiple galaxy–galaxy interactions (harassment) seem a likely mechanism for the dynamical transformation; however, the growth of the bulge does not appear to occur simultaneously. It is more likely that dynamical heating through tidal interactions occurs much later ($\geq$1 Gyr), after the molecular gas has been depleted and/or stripped. The current burst looks set to increase the mass of these galaxies by $\sim 1 \times 10^{10}$ $M_\odot$, with final stellar masses consistent with sub-M_* S0s. However, how this starburst episode may affect the bulge to disc ratio remains to be seen. To determine how much of the star formation is confined to central regions of the galaxy requires high-resolution millimetre/submillimetre observations, for example using ALMA.

5 CONCLUSIONS

At low redshift the effects of environment on the morphology, gas content and star formation of galaxies is a well-established phenomenon. Yet we know relatively little about the mechanisms which drive these trends, and how they depend on the properties of both the cluster, and the infalling galaxies on which they act. It is vital to develop a greater understanding of these issues if we are to explain the reversal of the morphology–density relation at high redshift.

In this study we investigated the dynamics, star formation and gas properties of 27 cluster starbursts from Cl 0024+17 ($z \sim 0.4$), to learn more about the nature of these galaxies, and how dense environments at high redshift can promote star formation in some infalling galaxies. This problem is key to explaining the early and rapid formation of today's massive cluster galaxies. Our main findings are as follows.

(i) We use deblended *Herschel* PACS/SPIRE maps to derive bolometric luminosities of $L_{IR} = (0.47–2.47) \times 10^{11}$ $L_\odot$ and star formation rates $SFR_{IR} = 5–26$ $M_\odot yr^{-1}$. The enhanced activity of these galaxies places them above the star-forming 'main sequence' for this redshift and stellar mass (an average of $\sim 3 \times 10^{10}$ $M_\odot$).

(ii) From the far-infrared photometry, we derive characteristic dust temperatures of $T_d = 26 \pm 1$ K, consistent with the local L_{IR}–T_d relation for field galaxies. We do not find any evidence that the cold gas/dust has been stripped by the interaction of the galaxy ISM with the ICM. If such an interaction occurs, then it must act on a much longer time-scale, or occur after the initial burst.

(iii) We search for the ^{12}CO $J(1\rightarrow0)$ emission from 11 galaxies in our sample. Of these targets, eight are within Cl 0024+17 and three within the foreground subgroup. Only two of eight galaxies are detected in the larger structure, while all three galaxies in the foreground group are detected at $>5\sigma$. We find the average ^{12}CO-derived gas mass of the sample (stacking detections and non-detections) to be $\sim 1 \times 10^{10}$ $M_\odot$. A median SFR of ~ 13 $M_\odot$ yr^{-1} suggests gas depletion time-scales of $\sim$1 Gyr, which is $\sim$0.25 of the cluster crossing time. Our galaxies appear to be richer in star-forming gas than typical field galaxies at the same redshift.

(iv) We use FLAMES multi-IFU data to study the ionized gas dynamics of these cluster starbursts, as traced by Hα emission, and after excluding AGN we find the majority of the sample ($\sim$90 per cent) have dynamics that appear to be consistent with undisturbed, uniformly rotating discs. To quantify the ratio between rotation and pressure support we calculate v/σ_0. The average for our sample is $v/\sigma_0 = 5 \pm 2$, in line with spirals of a similar redshift, further demonstrating that these galaxies have only recently accreted from the field.

(v) We also measure the spin, λ_R (a proxy for specific angular momentum) and concentration, c of the cluster starbursts. The relation between λ_R and c provides a useful means to follow the morphological and dynamical evolution of these galaxies. We derive a median spin and concentration of $\lambda_R = 0.83 \pm 0.06$ and $c = 2.1 \pm 0.3$, respectively. These values are consistent with typical field spirals. In order to evolve to S0s, these galaxies must double their concentration (through growth of the bulge) and decrease their angular momentum by a factor of $\sim$1.5.

(vi) Although limited by small numbers, galaxies in the subgroup do not show evidence of an accelerated evolution. The only difference between the 'main' cluster and subgroup components is (potentially) in the molecular gas properties, where all three subgroup members are detected in ^{12}CO but only two of eight galaxies are detected in the larger structure.

It appears that these dusty, star-forming galaxies must have only recently been accreted to the cluster, with their dynamics, morphologies and molecular gas consistent with star-forming field galaxies. They show no evidence of having yet been significantly disrupted by the dense environment. We conclude that for these $z \sim 0.4$ cluster galaxies to make the transition to S0s they must undergo a dynamical heating of the disc, and an increase in concentration. While ICM-related processes such as ram pressure stripping will truncate the gas disc, the full transformation from spiral to S0 is unlikely to be achieved by this process alone. Of the various available mechanisms, galaxy–galaxy encounters within the cluster seems most probable. Since $\sim$90 per cent of our sample display disc-like dynamics, it seems that this must occur after the initial burst has been quenched, and without an associated starburst.

ACKNOWLEDGEMENTS

We are grateful to the anonymous referee for useful comments. FLAMES IFU data employed in this analysis are from VLT programs 089.A-0983 and 092.A-0135, and are available through the ESO archive. HLJ, CMH, AMS, RGB, and IRS gratefully acknowledge support from the STFC (ST/K501979, ST/I001573/1 and ST/L00075X/1). IRS also acknowledges support from an ERC Advanced Investigator programme DUSTYGAL (321334) and a Royal Society Wolfson Merit Award. JEG acknowledges the support of the Royal Society.

REFERENCES

Alberts S. et al., 2014, MNRAS, 437, 437
Bamford S. P. et al., 2009, MNRAS, 393, 1324
Bekki K., 2009, MNRAS, 399, 2221
Bekki K., 2014, MNRAS, 438, 444
Bekki K., Couch W. J., 2011, MNRAS, 415, 1783
Bellocchi E., Arribas S., Colina L., Miralles-Caballero D., 2013, A&A, 557, A59
Bialas D., Lisker T., Olczak C., Spurzem R., Kotulla R., 2015, A&A, 576, A103
Bolzonella M., Miralles J.-M., Pelló R., 2000, A&A, 363, 476
Boselli A., Gavazzi G., 2006, PASP, 118, 517
Boselli A., Gavazzi G., 2014, A&AR, 22, 74
Bower R. G., Lucey J. R., Ellis R. S., 1992, MNRAS, 254, 601

Bruzual G., Charlot S., 2003, MNRAS, 344, 1000
Burstein D., Ho L. C., Huchra J. P., Macri L. M., 2005, ApJ, 621, 246
Butcher H., Oemler A., Jr, 1978, ApJ, 219, 18
Calzetti D., Armus L., Bohlin R. C., Kinney A. L., Koornneef J., Storchi-Bergmann T., 2000, ApJ, 533, 682
Cappellari M. et al., 2011, MNRAS, 416, 1680
Chapin E. L., Hughes D. H., Aretxaga I., 2009, MNRAS, 393, 653
Chapman S. C., Helou G., Lewis G. F., Dale D. A., 2003, ApJ, 588, 186
Chary R., Elbaz D., 2001, ApJ, 556, 562
Christlein D., Zabludoff A. I., 2004, ApJ, 616, 192
Coia D. et al., 2005, A&A, 431, 433
Colina L., Arribas S., Monreal-Ibero A., 2005, ApJ, 621, 725
Combes F., García-Burillo S., Braine J., Schinnerer E., Walter F., Colina L., 2013, A&A, 550, A41
Comerford J. M., Meneghetti M., Bartelmann M., Schirmer M., 2006, ApJ, 642, 39
Cortesi A. et al., 2013, MNRAS, 432, 1010
Couch W. J., Sharples R. M., 1987, MNRAS, 229, 423
Courteau S., 1997, AJ, 114, 2402
Czoske O., Kneib J.-P., Soucail G., Bridges T. J., Mellier Y., Cuillandre J.-C., 2001, A&A, 372, 391
Czoske O., Moore B., Kneib J.-P., Soucail G., 2002, A&A, 386, 31
De Lucia G., Poggianti B. M., Halliday C., Milvang-Jensen B., Noll S., Smail I., Zaritsky D., 2009, MNRAS, 400, 68
Diaferio A., Geller M. J., Rines K. J., 2005, ApJ, 628, L97
Draine B. T. et al., 2007, ApJ, 663, 866
Dressler A., 1980, ApJ, 236, 351
Dressler A. et al., 1997, ApJ, 490, 577
Elbaz D. et al., 2007, A&A, 468, 33
Eliche-Moral M. C., González-García A. C., Aguerri J. A. L., Gallego J., Zamorano J., Balcells M., Prieto M., 2012, A&A, 547, A48
Emsellem E. et al., 2011, MNRAS, 414, 888
Fogarty L. M. R. et al., 2015, MNRAS, 454, 2050
Freeman K. C., 1970, ApJ, 160, 811
Fumagalli M., Fossati M., Hau G. K. T., Gavazzi G., Bower R., Sun M., Boselli A., 2014, MNRAS, 445, 4335
Gao Y., Solomon P. M., 2004, ApJ, 606, 271
Geach J. E. et al., 2006, ApJ, 649, 661
Geach J. E., Smail I., Moran S. M., Treu T., Ellis R. S., 2009, ApJ, 691, 783
Geach J. E., Smail I., Moran S. M., MacArthur L. A., Lagos C. d. P., Edge A. C., 2011, ApJ, 730, L19
Genzel R. et al., 2015, ApJ, 800, 20
Guilloteau S., Lucas R., 2000, in Mangum J. G., Radford S. J. E., eds, ASP Conf. Ser. Vol. 217, Imaging at Radio through Submillimeter Wavelengths. Astron. Soc. Pac., San Francisco, p. 299
Harrison C. M. et al., 2016, MNRAS, 456, 1195
Hoekstra H., 2007, MNRAS, 379, 317
Hogg D. W., Masjedi M., Berlind A. A., Blanton M. R., Quintero A. D., Brinkmann J., 2006, ApJ, 650, 763
Hopkins P. F., Hernquist L., Cox T. J., Di Matteo T., Robertson B., Springel V., 2006, ApJS, 163, 1
Hung C.-L., Hayward C. C., Smith H. A., Ashby M. L. N., Lanz L., Martínez-Galarza J. R., Sanders D. B., Zezas A., 2016, ApJ, 816, 99
Ivison R. J. et al., 2013, ApJ, 772, 137
Johnston E. J., Aragón-Salamanca A., Merrifield M. R., 2014, MNRAS, 441, 333
Karim A. et al., 2011, ApJ, 730, 61
Kassin S. A. et al., 2012, ApJ, 758, 106
Kenney J. D. P., van Gorkom J. H., Vollmer B., 2004, AJ, 127, 3361
Kennicutt R. C., Jr, 1998, ApJ, 498, 541
Kewley L. J., Dopita M. A., Leitherer C., Davé R., Yuan T., Allen M., Groves B., Sutherland R., 2013, ApJ, 774, 100
Kneib J.-P. et al., 2003, ApJ, 598, 804
Kocevski D. D. et al., 2011, ApJ, 736, 38
Kodama T., Smail I., 2001, MNRAS, 326, 637
Kodama T., Balogh M. L., Smail I., Bower R. G., Nakata F., 2004, MNRAS, 354, 1103
Koyama Y. et al., 2008, MNRAS, 391, 1758
Leitherer C. et al., 2011, Astrophysics Source Code Library, ascl:1104.003
Lewis I. et al., 2002, MNRAS, 334, 673
Lutz D. et al., 2011, A&A, 532, A90
Ma C.-J. et al., 2015, ApJ, 806, 257
McCarthy I. G., Frenk C. S., Font A. S., Lacey C. G., Bower R. G., Mitchell N. L., Balogh M. L., Theuns T., 2008, MNRAS, 383, 593
Marcillac D., Rigby J. R., Rieke G. H., Kelly D. M., 2007, ApJ, 654, 825
Mastropietro C., Moore B., Mayer L., Debattista V. P., Piffaretti R., Stadel J., 2005, MNRAS, 364, 607
Merluzzi P. et al., 2013, MNRAS, 429, 1747
Mihos J. C., Bothun G. D., 1998, ApJ, 500, 619
Moran S. M., Ellis R. S., Treu T., Smail I., Dressler A., Coil A. L., Smith G. P., 2005, ApJ, 634, 977
Moran S. M., Miller N., Treu T., Ellis R. S., Smith G. P., 2007, ApJ, 659, 1138
Muzzin A. et al., 2013, ApJ, 777, 18
Noeske K. G. et al., 2007, ApJ, 660, L43
Oemler A., Jr, Dressler A., Kelson D., Rigby J., Poggianti B. M., Fritz J., Morrison G., Smail I., 2009, ApJ, 693, 152
Oliver S. J. et al., 2012, MNRAS, 424, 1614
Ota N., Pointecouteau E., Hattori M., Mitsuda K., 2004, ApJ, 601, 120
Peng Y., Maiolino R., Cochrane R., 2015, Nature, 521, 192
Poggianti B. M., Wu H., 2000, ApJ, 529, 157
Poggianti B. M., Smail I., Dressler A., Couch W. J., Barger A. J., Butcher H., Ellis R. S., Oemler A. J., 1999, ApJ, 518, 576
Poggianti B. M. et al., 2009, ApJ, 693, 112
Pracy M. B., Couch W. J., Blake C., Bekki K., Harrison C., Colless M., Kuntschner H., de Propris R., 2005, MNRAS, 359, 1421
Puech M., Hammer F., Lehnert M. D., Flores H., 2007, A&A, 466, 83
Querejeta M. et al., 2015, A&A, 579, L2
Quilis V., Moore B., Bower R., 2000, Science, 288, 1617
Rawle T. D. et al., 2012, ApJ, 756, 106
Rieke G. H., Alonso-Herrero A., Weiner B. J., Pérez-González P. G., Blaylock M., Donley J. L., Marcillac D., 2009, ApJ, 692, 556
Rodríguez Del Pino B., Bamford S. P., Aragón-Salamanca A., Milvang-Jensen B., Merrifield M. R., Balcells M., 2014, MNRAS, 438, 1038
Sales L. V. et al., 2015, MNRAS, 447, L6
Sandage A., 2005, ARA&A, 43, 581
Simien F., de Vaucouleurs G., 1986, ApJ, 302, 564
Smail I. et al., 2014, ApJ, 782, 19
Smith G. P., Treu T., Ellis R. S., Moran S. M., Dressler A., 2005, ApJ, 620, 78
Smith R., Davies J. I., Nelson A. H., 2010, MNRAS, 405, 1723
Solomon P. M., Vanden Bout P. A., 2005, ARA&A, 43, 677
Soucail G., Ota N., Böhringer H., Czoske O., Hattori M., Mellier Y., 2000, A&A, 355, 433
Stott J. P. et al., 2016, MNRAS, 457, 1888
Swinbank A. M. et al., 2007, MNRAS, 379, 1343
Swinbank A. M. et al., 2014, MNRAS, 438, 1267
Symeonidis M. et al., 2013, MNRAS, 431, 2317
Tacconi L. J. et al., 2010, Nature, 463, 781
Tran K.-V. H., Franx M., Illingworth G. D., van Dokkum P., Kelson D. D., Blakeslee J. P., Postman M., 2007, ApJ, 661, 750
Tran K.-V. H. et al., 2010, ApJ, 719, L126
Treu T., Ellis R. S., Kneib J.-P., Dressler A., Smail I., Czoske O., Oemler A., Natarajan P., 2003, ApJ, 591, 53
Umetsu K., Medezinski E., Broadhurst T., Zitrin A., Okabe N., Hsieh B.-C., Molnar S. M., 2010, ApJ, 714, 1470
Vulcani B. et al., 2011, MNRAS, 412, 246
Wisnioski E. et al., 2015, ApJ, 799, 209
Wuyts S. et al., 2013, ApJ, 779, 135
Zhang Y.-Y., Böhringer H., Mellier Y., Soucail G., Forman W., 2005, A&A, 429, 85
Zitrin A. et al., 2009, MNRAS, 396, 1985

APPENDIX A: ADDITIONAL MATERIAL

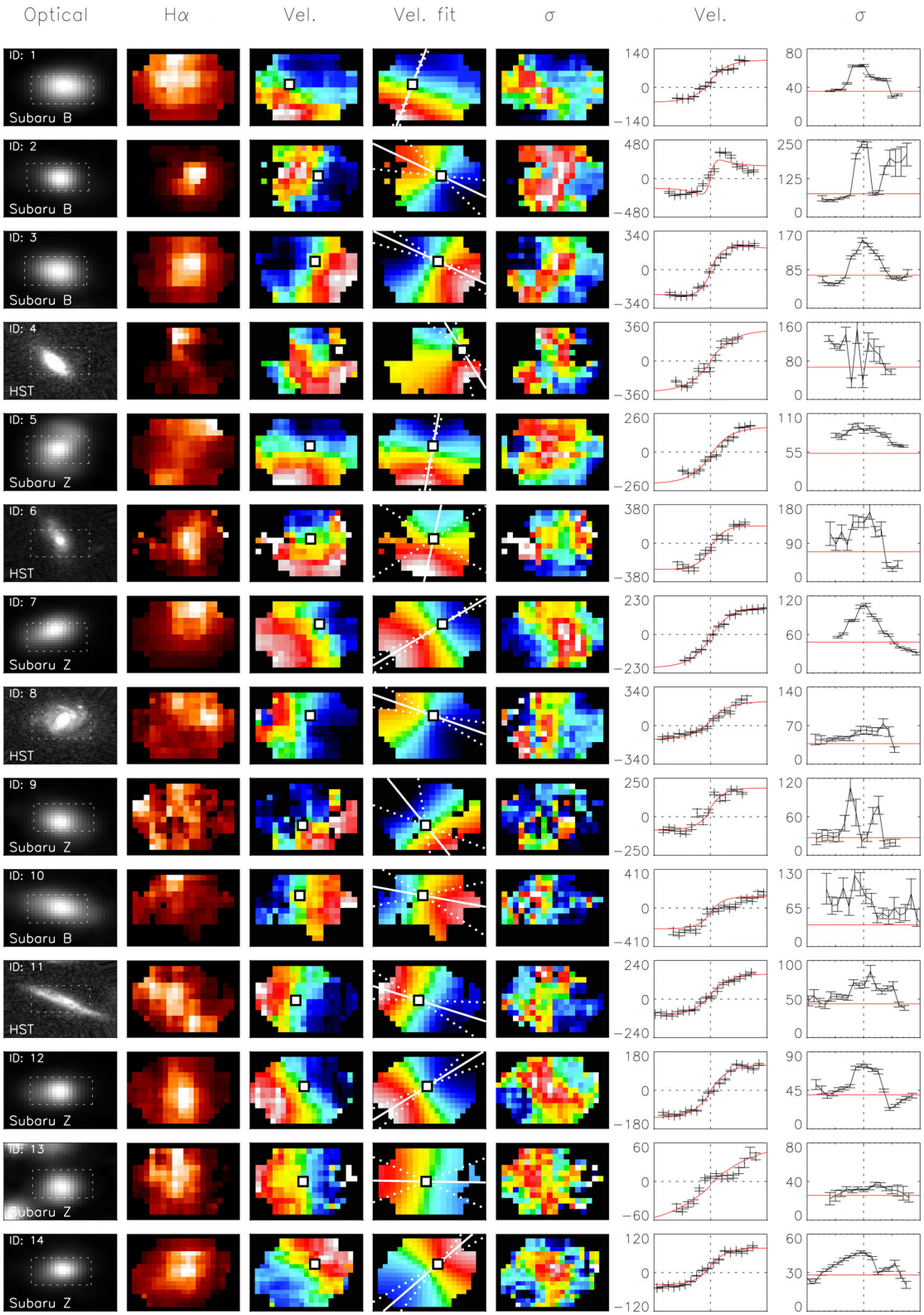

Figure A1. Broad-band image, Hα morphology and dynamical maps for all 27 galaxies in our cluster starburst sample. Left to right we show: Subaru or *HST* broad-band image (dashed lines illustrate the FLAMES field of view), Hα intensity map, velocity field, best-fitting model velocity field, dispersion map, and the rotation curve (red line is the model fit) and line-of-sight dispersion profile (red line is σ_0) extracted along the primary axis. Axes are in units of km s^{-1}. The solid line on the velocity field shows the position angle, with dashed lines illustrating the 1σ uncertainty. Square points show the model dynamical centre.

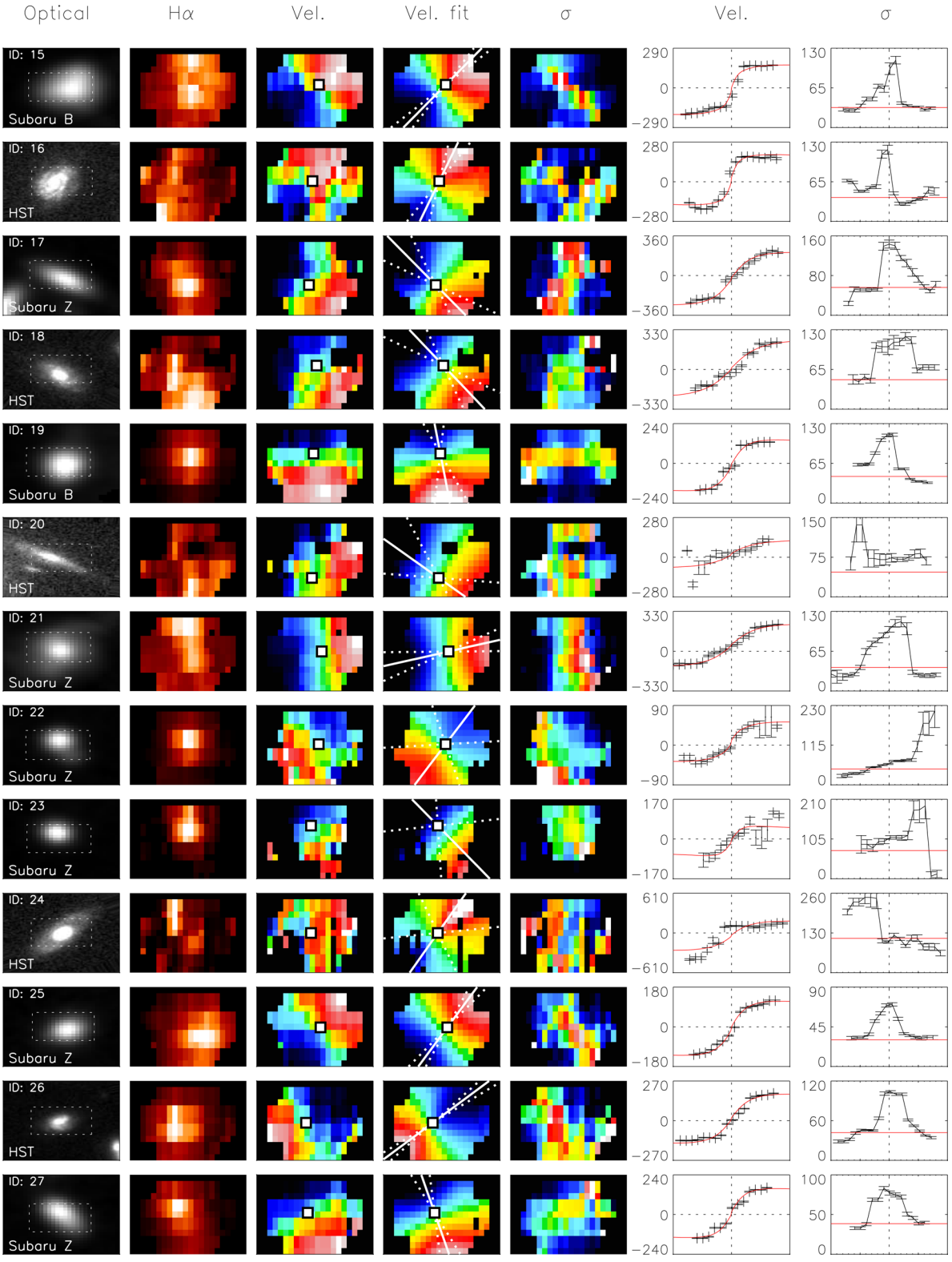

Figure A1 – *continued.*

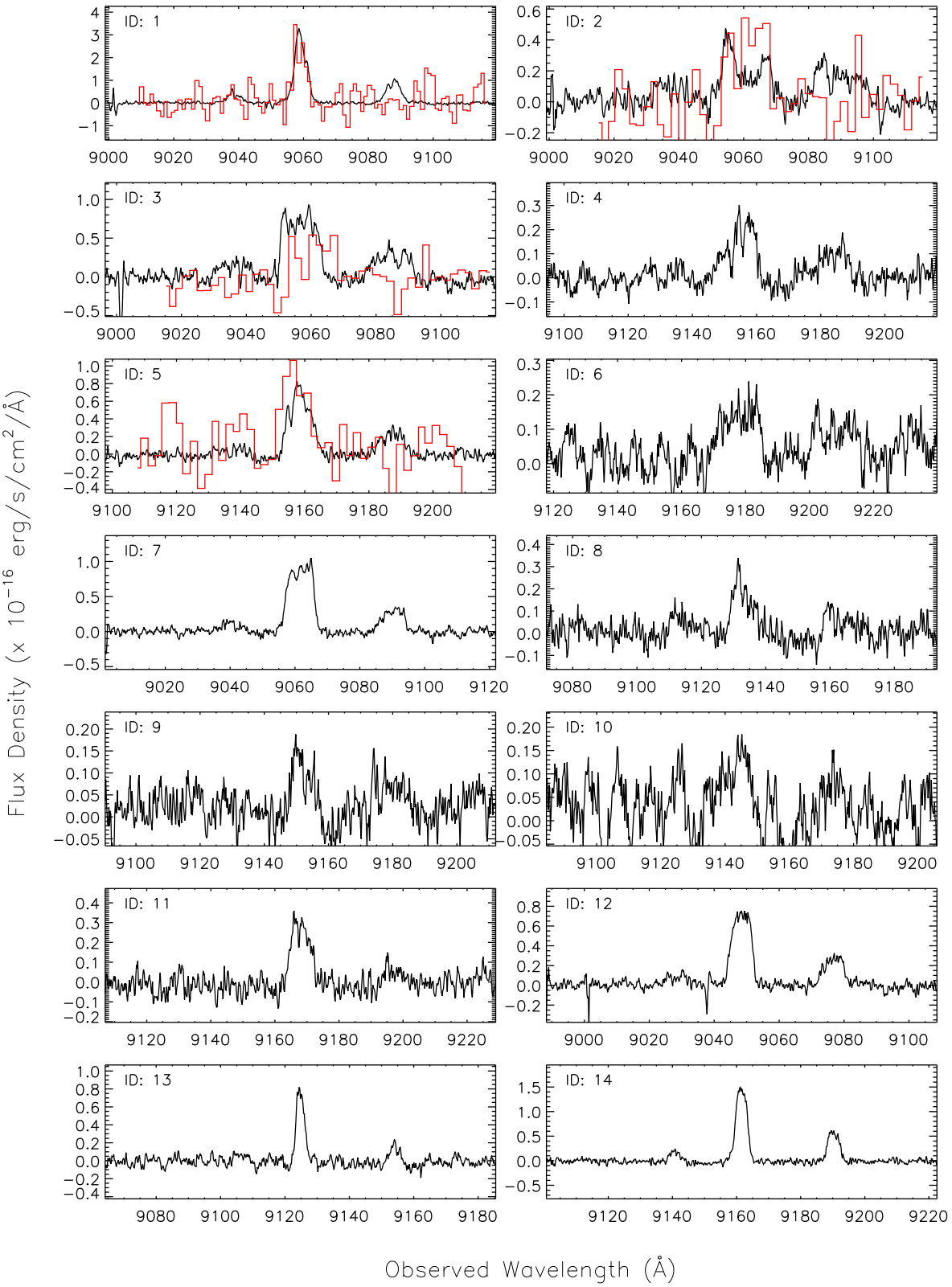

Figure A2. Integrated spectra around redshifted Hα and [N II] (6548,6583) emission lines. Parameters such as redshifts and [N II]/Hα ratios are listed in Table A1. Many galaxies show split emission line profiles, indicative of high-velocity rotation and possibly strong obscuration towards the dynamical centre. We suspect the dynamics of galaxy IDs 23 and 24 may be affected by an AGN. For IDs 1, 2, 3, 5 and 16 we overlay the CO spectra in red, and find that the velocity centroid and line width are well matched to the Hα emission.

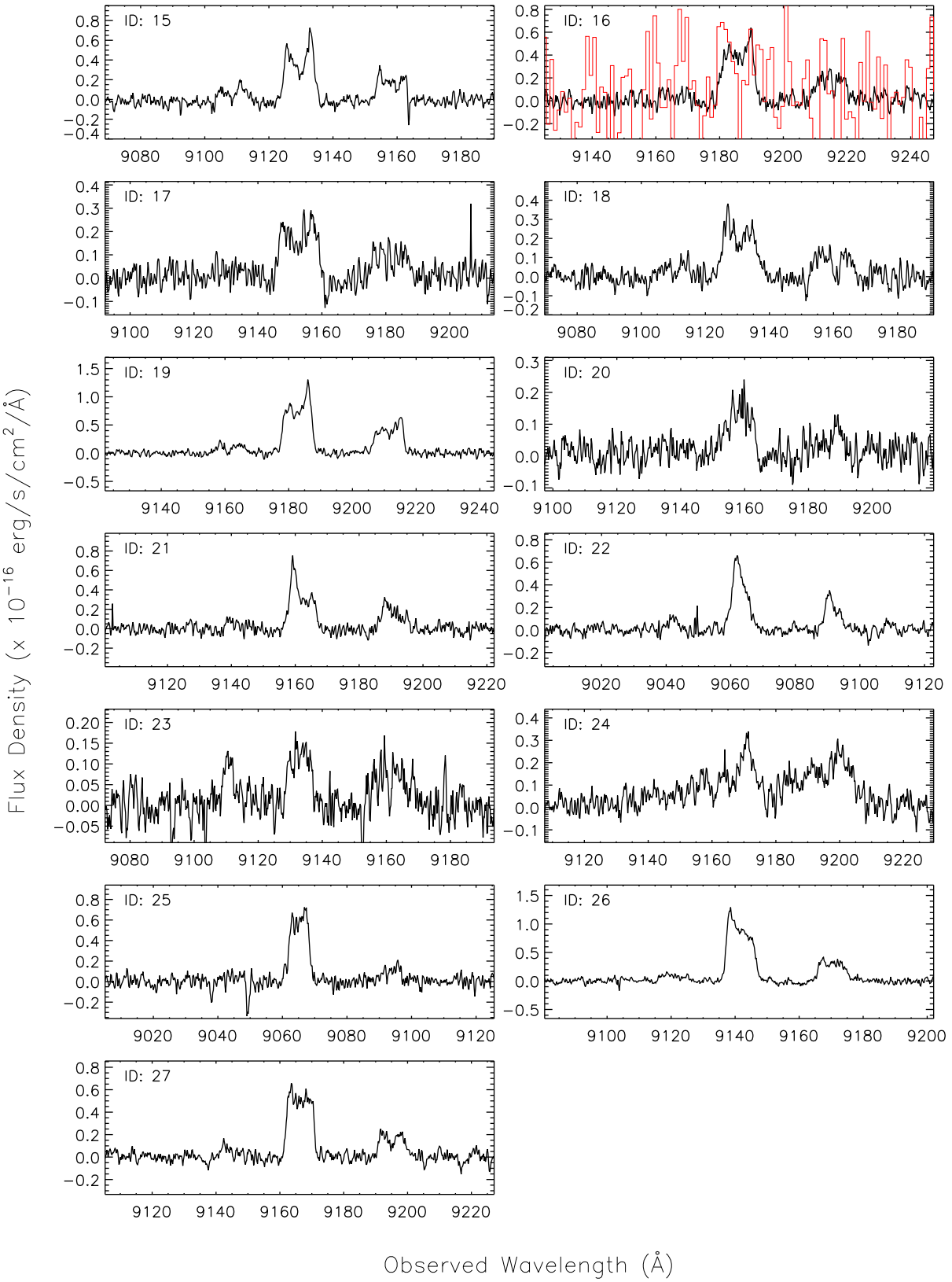

Figure A2 – *continued.*

Table A1. Observed properties.

ID	RA (J2000)	Dec (J2000)	$z_{\mathrm{H}\alpha}$	S_{24} (μJy)	$f_{\mathrm{H}\alpha}$ (10^{-16} erg s^{-1})	log([N II]/Hα)	B (AB)	R (AB)	Subgroup
1	6.59050	17.3240	0.3804	950 ± 40	14.0 ± 0.2	-0.48 ± 0.01	21.63	19.80	y
2	6.81270	17.2131	0.3804	950 ± 50	4.2 ± 0.2	-0.11 ± 0.03	22.53	19.98	y
3	6.71870	17.2332	0.3800	830 ± 20	10.6 ± 0.3	-0.37 ± 0.02	22.31	20.10	y
4	6.53730	17.2530	0.3950	770 ± 30	2.2 ± 0.1	-0.28 ± 0.04	23.88	21.32	n
5	6.76520	17.1912	0.3955	706 ± 50	6.1 ± 0.1	-0.44 ± 0.02	22.42	20.45	n
6	6.60820	17.2976	0.3986	440 ± 20	1.5 ± 0.1	-0.24 ± 0.06	24.03	21.34	n
7	6.75580	17.3446	0.3808	350 ± 30	8.5 ± 0.2	-0.52 ± 0.01	22.16	20.48	y
8	6.66020	17.1254	0.3916	201 ± 5	1.50 ± 0.08	-0.38 ± 0.06	22.98	20.76	n
9	6.55990	17.2222	0.3944	< 150	0.83 ± 0.07	-0.29 ± 0.07	23.36	21.15	n
10	6.66080	17.2539	0.3935	< 150	0.72 ± 0.08	-0.22 ± 0.07	23.28	20.95	n
11	6.64020	17.2055	0.3970	350 ± 50	2.30 ± 0.08	-0.67 ± 0.06	23.57	21.71	n
12	6.58330	17.0687	0.3788	670 ± 40	5.27 ± 0.09	-0.42 ± 0.01	22.86	21.00	y
13	6.60210	17.1917	0.3904	290 ± 30	2.51 ± 0.06	-0.58 ± 0.05	23.09	21.43	n
14	6.65550	17.0162	0.3960	600 ± 30	6.44 ± 0.08	-0.39 ± 0.01	22.40	20.52	n
15	6.67300	17.1838	0.3911	311 ± 5	4.7 ± 0.2	-0.30 ± 0.04	22.26	20.10	n
16	6.63200	17.1545	0.3997	227 ± 4	5.1 ± 0.2	-0.35 ± 0.03	22.86	20.80	n
17	6.66270	17.1672	0.3947	214 ± 4	2.5 ± 0.1	-0.36 ± 0.05	23.91	21.42	n
18	6.63970	17.1566	0.3913	179 ± 4	3.1 ± 0.1	-0.30 ± 0.03	23.01	20.80	n
19	6.69910	17.1619	0.3993	307 ± 7	8.9 ± 0.2	-0.27 ± 0.02	22.13	20.17	n
20	6.52550	17.2054	0.3955	300 ± 50	1.33 ± 0.08	-0.44 ± 0.06	23.92	21.71	n
21	6.74790	17.0626	0.3960	280 ± 30	3.8 ± 0.1	-0.34 ± 0.03	22.53	20.51	n
22	6.63740	17.2581	0.3809	345 ± 30	3.05 ± 0.06	-0.36 ± 0.02	23.35	21.29	y
23	6.72500	17.2343	0.3916	300 ± 30	1.11 ± 0.07	-0.02 ± 0.04	23.79	21.03	n
24	6.58090	17.1174	0.3970	340 ± 30	3.1 ± 0.2	0.04 ± 0.03	23.46	20.69	n
25	6.64270	17.1011	0.3813	260 ± 30	4.5 ± 0.1	-0.69 ± 0.04	22.89	21.26	y
26	6.60710	17.2015	0.3929	340 ± 40	9.4 ± 0.2	-0.46 ± 0.03	22.30	20.53	n
27	6.65550	17.1768	0.3967	158 ± 5	5.2 ± 0.1	-0.49 ± 0.03	23.11	21.21	n

Notes. The *B*- and *R*-band magnitudes were extracted at the same aperture, in order to derive the colours plotted in Fig. 2. In the final column, we specify whether each galaxy is a member of the 'main' cluster (n) or foreground subgroup (y), as discussed in Section 2.1.

Table A2. Derived properties – Galaxy integrated.

ID	L_{IR} (10^{11} L$_\odot$)	$\mathrm{SFR_{IR}}$ (M$_\odot$ yr^{-1})	T_{d} (K)	M_{K} (AB)	$M_\star$ (10^{10} M$_\odot$)	L'_{CO} (10^9 K km s^{-1} pc^2)	M_{gas} (10^{10} M$_\odot$)
1	2.5^{+2}_{-3}	26^{+3}_{-13}	29 ± 11	-22.8	5.6 ± 2.5	6.8 ± 0.6	3.1 ± 0.3
2	$0.5^{+0.9}_{-0.3}$ *	11^{+2}_{-2}	> 20	-23.4	9.6 ± 2.9	2.6 ± 0.3	1.2 ± 0.3
3	$1.4^{+1.5}_{-1.2}$	14^{+2}_{-1}	25 ± 12	-23.0	6.8 ± 2.0	6.4 ± 0.5	2.9 ± 0.2
4	1.3^{+2}_{-1}	13^{+9}_{-2}	> 18	-22.5	4.1 ± 1.2	< 3.9	< 1.8
5	$0.6^{+0.8}_{-0.4}$	6^{+3}_{-1}	> 23	-22.2	3.0 ± 1.4	4.3 ± 0.6	2.0 ± 0.3
6	$0.5^{+0.9}_{-0.3}$ *	10^{+2}_{-2}	31 ± 22	-22.4	3.7 ± 1.1	–	–
7	$0.9^{+1.0}_{-0.8}$	10^{+1}_{-2}	> 11	-21.8	2.1 ± 0.8	–	–
8	$0.8^{+0.9}_{-0.7}$	8^{+1}_{-1}	24 ± 2	-22.2	3.2 ± 1.0	–	–
9	$0.8^{+0.9}_{-0.7}$	8^{+1}_{-1}	> 11	-21.7	1.9 ± 0.6	–	–
10	$0.6^{+0.7}_{-0.5}$	6^{+1}_{-1}	> 11	-22.1	2.9 ± 0.9	–	–
11	1.6^{+3}_{-1}	17^{+13}_{-3}	25 ± 1	-21.3	1.4 ± 0.5	–	–
12	$1.0^{+1}_{-0.9}$	11^{+1}_{-2}	> 15	-21.9	2.5 ± 0.9	–	–
13	$0.5^{+1}_{-0.4}$ *	3^{+1}_{-1}	24 ± 2	-20.9	1.0 ± 0.4	< 4.3	< 2.0
14	$0.5^{+1}_{-0.4}$ *	17^{+3}_{-3}	> 11	-22.1	2.8 ± 1.1	–	–
15	$0.6^{+2}_{-0.4}$ *	9^{+2}_{-2}	28 ± 1	-22.6	4.6 ± 2.1	–	–
16	$0.5^{+1}_{-0.4}$ *	11^{+2}_{-2}	26 ± 1	-22.0	2.6 ± 1.2	2.2 ± 0.7	1.0 ± 0.3
17	$0.5^{+2}_{-0.1}$ *	12^{+2}_{-2}	26 ± 1	-22.0	2.5 ± 1.2	< 4.4	< 2.0
18	$0.5^{+0.9}_{-0.3}$ *	5^{+1}_{-1}	27 ± 2	-22.1	2.8 ± 0.9	< 4.1	< 1.9
19	1.2^{+1}_{-1}	13^{+1}_{-3}	26 ± 2	-22.7	5.0 ± 1.8	–	–
20	0.9^{+5}_{-1}	20^{+31}_{-9}	> 11	-21.7	2.1 ± 0.9	–	–
21	$0.6^{+0.7}_{-0.5}$	6^{+1}_{-1}	> 11	-22.3	3.4 ± 1.7	–	–
22	$1.0^{+4}_{-0.9}$	11^{+35}_{-1}	> 11	-21.5	1.7 ± 0.8	–	–

Table A2 – *continued.*

ID	L_{IR} (10^{11} $L_\odot$)	SFR_{IR} ($M_\odot$ yr^{-1})	T_d (K)	M_K (AB)	$M_\star$ (10^{10} $M_\odot$)	L'_{CO} (10^9 K km s^{-1} pc^2)	M_{gas} (10^{10} $M_\odot$)
23	1.3^{+2}_{-1}	14^{+7}_{-4}	> 11	-21.7	2.0 ± 0.6	–	–
24	$1.3^{+2}_{-0.6}$	13^{+7}_{-6}	> 11	-22.6	4.5 ± 1.4	–	–
25	$0.5^{+0.5}_{-0.5}$ *	6^{+2}_{-2}	> 11	-21.0	1.1 ± 0.4	–	–
26	$0.6^{+0.6}_{-0.6}$	6^{+1}_{-2}	30 ± 2	-22.1	2.8 ± 1.3	< 4.9	< 2.3
27	$0.5^{+0.9}_{-0.4}$ *	8^{+2}_{-2}	27 ± 2	-21.3	1.3 ± 0.6	< 4.6	< 2.1

Notes. L_{IR} is the bolometric luminosity of the best-fitting template SED fit to *Herschel* far-infrared photometry. SFR with an adjacent ⋆ were derived by applying the average $SFR_{H\alpha}/SFR_{IR}$ correction factor, since these galaxies have detections in only ≤ 1 bands. The characteristic dust temperatures, T_d, come from a single-temperature blackbody fit, assuming an emissivity index of $\beta = 1.8$. Stellar mass estimates were calculated using a constant mass-to-light ratio of $M_\odot/L^K_\odot = 0.35$. L'_{CO} and M_{gas} are derived from a Gaussian fit to IRAM/NOEMA CO(1−0) spectra (see Section 3.4), for which we assume a CO to H_2 conversion factor of $\alpha = 4.6$.

Table A3. Derived properties – ionized gas dynamics.

ID	σ_0 (km s^{-1})	$r_{1/2}$ (kpc)	$v_{2.2}$ (km s^{-1})	$v_{2.2}/\sigma_0$	λ_R	Class
1	36 ± 5	6.0 ± 0.4	120 ± 10	3.4 ± 0.5	0.71 ± 0.02	R
2	76 ± 8	6.2 ± 0.5	210 ± 40	2.8 ± 0.7	0.74 ± 0.01	R
3	72 ± 5	5.5 ± 0.4	270 ± 20	3.7 ± 0.5	0.77 ± 0.01	R
4	67 ± 5	8.5 ± 0.4	300 ± 20	4.4 ± 0.6	0.82 ± 0.01	I
5	53 ± 5	8.5 ± 0.5	230 ± 10	4.3 ± 0.5	0.82 ± 0.01	R
6	70 ± 9	9.6 ± 0.5	310 ± 20	4 ± 2	0.83 ± 0.01	R
7	48 ± 5	6.0 ± 0.5	280 ± 30	5.7 ± 0.9	0.83 ± 0.02	R
8	37 ± 5	5.8 ± 0.5	260 ± 50	7 ± 2	0.90 ± 0.02	R
9	28 ± 7	5.9 ± 0.4	210 ± 60	8 ± 2	0.85 ± 0.03	R
10	37 ± 7	9.5 ± 0.4	190 ± 20	5.3 ± 0.8	0.87 ± 0.01	R
11	44 ± 5	9.8 ± 0.5	140 ± 10	3.2 ± 0.5	0.83 ± 0.01	R
12	40 ± 5	5.0 ± 0.4	250 ± 50	6 ± 2	0.82 ± 0.07	R
13	26 ± 5	5.4 ± 0.6	130 ± 40	5 ± 2	0.72 ± 0.02	R
14	28 ± 5	6.9 ± 0.2	100 ± 10	3.4 ± 0.6	0.74 ± 0.03	R
15	33 ± 5	6.0 ± 0.4	300 ± 20	8 ± 1	0.90 ± 0.02	R
16	40 ± 4	5.7 ± 0.4	200 ± 10	5.0 ± 0.7	0.77 ± 0.04	R
17	57 ± 7	6.8 ± 0.8	290 ± 30	5.1 ± 0.8	0.86 ± 0.01	R
18	48 ± 5	6.0 ± 0.6	290 ± 30	6 ± 1	0.86 ± 0.05	R
19	44 ± 4	4.2 ± 0.3	220 ± 40	5 ± 1	0.79 ± 0.03	R
20	47 ± 6	8.8 ± 0.7	130 ± 30	2.8 ± 0.7	0.86 ± 0.01	I
21	40 ± 4	9.7 ± 0.4	230 ± 20	5.9 ± 0.8	0.76 ± 0.03	R
22	46 ± 5	5.2 ± 0.5	150 ± 20	3 ± 3	0.69 ± 0.02	I
23	75 ± 6	4.0 ± 0.4	90 ± 30	1.2 ± 0.4	0.47 ± 0.01	I
24	112 ± 7	8.0 ± 0.3	230 ± 20	2.0 ± 0.3	0.47 ± 0.03	I
25	30 ± 5	6.0 ± 0.4	220 ± 20	7 ± 1	0.92 ± 0.05	R
26	42 ± 4	3.7 ± 0.5	190 ± 10	4.5 ± 0.5	0.75 ± 0.06	R
27	38 ± 5	5.8 ± 0.4	200 ± 30	5.2 ± 0.8	0.86 ± 0.04	R

Notes. To estimate the intrinsic velocity dispersion, σ_0, we correct the two-dimensional σ map for beam smearing and instrumental broadening, then take a pixel-by-pixel mean which is inverse weighted by the error. The rotational support, v/σ_0, is calculated using the value of the rotation curve at $2.2 \times r_{1/2}$ ($v_{2.2}$ and $r_{2.2}$, respectively), corrected for the inclination of the disc. The spin parameter, λ_R, is calculated using all pixels within the half-light radius (see Section 4.3). The final column describes the dynamical class we assign, taking into account the two-dimensional dynamical maps, optical morphology, rotation curve and line-of-sight velocity dispersion profile – 'R' if the galaxy resembles an undisturbed, rotating disc, and 'I' if the galaxy shows some sign of irregular kinematics or merger activity. We note that IDs 23 and 24 likely have an AGN which is disturbing the gas dynamics.

This paper has been typeset from a TEX/LATEX file prepared by the author.